TERRESTRIAL RECORD OF CYCLIC EARLY EOCENE WARM-HUMID EVENTS IN CLAY MINERAL ASSEMBLAGES FROM THE SALTA BASIN, NORTHWESTERN ARGENTINA

MARGARITA DO CAMPO[a], BLANCA BAULUZ[b], CECILIA DEL PAPA[c], PATRICIO PAYROLA[d], ALFONSO YUSTE[b], MARIA JOSE MAYAYO[b]

[a] Universidad de Buenos Aires, Facultad de Ciencias Exactas y Naturales and INGEIS (CONICET – UBA), Ciudad Universitaria, Intendente Güiraldes s/n (1428) Buenos Aires, Argentina. Email: docampo@ingeis.uba.ar

[b] IUCA-Departamento de Ciencias de la Tierra, Universidad de Zaragoza, Pedro Cerbuna 12, (500009) Zaragoza, Spain. Emails: bauluz@unizar.es, alfon@unizar.es, mayayo@unizar.es.

[c] CICTERRA, CONICET-Universidad Nacional de Córdoba, Av. Vélez Sarsfield 1699, X5016GCB Córdoba, Argentina. Email: delpapacecilia@yahoo.com

[d] IBIGEO, CONICET , Av. 9 de Julio 14, A4405BBA Rosario de Lerma, Salta, Argentina. Email: ppayrola@gmail.com

ABSTRACT

The Eocene continental sequence investigated in this study belongs to the Salta Group; it was deposited in an intracontinental rift, the Salta Basin (NW Argentina) that evolved from the Lower Cretaceous to middle Paleogene. The Salta Group contains the Maíz Gordo and Lumbrera Fms, spans the Paleocene-early Eocene, and shows excellent exposures in the region of the Valles Calchaquíes. This research is focused on the continental facies of the Lumbrera Fm, which correspond to the early Eocene. We studied the mineralogy of the fine-grained beds of the Lumbrera Fm in five locations (Valle Encantado, Tonco, Tin Tin, Luracatao, and Obelisco) by X-ray diffraction and scanning electron microscopy in order to examine the vertical variations in clay mineralogy and their relations with global paleoclimatic changes registered during the Eocene. The microtexture of the authigenic smectite-type clays (Sm to I/Sm R0) suggests that they mainly originated by crystallization from glassy volcanic materials. The high reactivity of the glass precludes the use of smectite-type-clay formation as an indicator of specific paleoclimatic conditions in the studied sediments. In contrast, the formation of kaolinite in sections with very low smectite proportions and a strong degree of weathering in crystalline silicates reflects intense weathering conditions and is a useful paleoclimatic proxy in terrestrial sediments. Significant variations in kaolinite/muscovite ratios at the base and in an intermediate bed in the Lumbrera Fm at Valle Encantado suggest the presence of cyclic hyperthermals through the Ypresian stage that may be tentatively correlated with the Eocene Thermal Maxima 2 and 3, which are the largest events that have been identified at a global scale in early Eocene marine sediments.

KEYWORDS: Paleoclimate reconstruction, continental basins, kaolinite, EECO

1. INTRODUCTION

From the late Paleocene (58 Ma) to the early Eocene the Earth's surface underwent a short period of warming associated with elevated levels of atmospheric CO_2; according to various lines of evidence, this was the warmest period in the Cenozoic Era (Kennett and Stott, 1991; Zachos et al., 1993, 2001; Schmitz and Pujalte, 2007; Sluijs et al., 2007; McInerney and Wing, 2011). This event, known as the Paleocene-Eocene thermal maximum (PETM or ETM-1), occurred ~56 million years ago in a short period of time that spanned ~170,000 years (Röhl et al., 2007; Westerhold, 2008; Charles et al., 2011; Zeebe et al., 2016). A few million years later there was another long-term warming trend forced by high concentrations of atmospheric CO_2, which comprises a period called the Early Eocene Climatic Optimum (EECO; ~53-49 Ma; Zachos et al., 2001, 2008; Kirtland Turner and Ridgwell, 2013; Lauretano et al., 2015, 2018; Westerhold et al., 2018; Crouch et al., 2020). This long-term trend through the Ypresian stage was punctuated by recurrent transient warming events, associated with carbon isotope excursions (CIEs), called "hyperthermals" (Thomas, 1998; Thomas et al., 2000; Zachos et al., 2010). The chronology of the different hyperthermals, their relationship with eccentricity cycles, as well as the evolution of surface and sea-bottom temperatures, have been established mainly from the study of deep-sea cores (Cramer et al., 2009; Zachos et al., 2010; Laurentano et al., 2015, 2018; Thomas et al., 2018; Westerhold, et al., 2018; Crouch et al., 2020). The hyperthermal events of the Paleocene-early Eocene were initially recognized in several deep-sea cores from the Atlantic Ocean (e.g., Cramer et al., 2003; Lauretano et al., 2015; Littler et al., 2014, 2010; Zachos et al., 2005, 2010), but were subsequently also identified in deep-sea cores from the Pacific Ocean as well as in marine sedimentary successions outcropping in various localities (Nicolo et al., 2007; Galeotti et al., 2017; Westerhold et al., 2018). Initially two warming events, ETM-2 and 3, were identified in the early Eocene (Zachos et al., 2010; Röhl et al., 2005), but the high-resolution analysis of deep-sea cores identified several prominent CIEs occurring between 55 and 52 Ma, which were labeled from E to L by Cramer et al. (2003) and have been correlated with short eccentricity cycle maxima. Recently, excursions H to L, as well as 20 additional smaller CIEs, have been documented for the Ypresian to early Lutetian (56–45 Ma) in stable isotope records from sea cores from the Demerara Rise in the equatorial Atlantic (Kirtland Turner and Ridgwell, 2013; Sexton et al., 2011; Laurentano et al., 2016). The paleoclimatic changes taking place during this period have been extensively studied in the last few decades since they are considered analogous to current global greenhouse conditions.

At the same time, the study of the climatic conditions prevailing during the early Eocene in terrestrial realms is crucial to understanding how the current global greenhouse climate could affect temperatures and hydrological cycles in inner continental areas. In fact, studies in different basins indicate that early Eocene hyperthermal events were associated with marked changes in hydrological cycles, which in turn modified surface processes such as the rate of erosion and chemical weathering (Clechenko et al., 2007; Schmitz and Pujalte, 2007; Bataille et al., 2019). However, our knowledge of continental climates during the Paleocene-early Eocene remains limited. There is a consensus that the global climate was warmer than at present during the Mesozoic and Early Cenozoic, but disagreements remain with respect to winter temperatures and latitudinal gradients, and also the consequences of warming events on hydrological cycles (Greenwood and Wing, 1995). These studies have applied different approaches to understanding the environmental conditions that prevailed during the early Eocene, including the use of carbon and oxygen isotope data, paleontological data (i.e., foliar physiognomy and floristic composition), the characterization of paleosols, the study of clay assemblages, and sedimentological evidence (Greenwood and Wing, 1995, 2010; Bataille et al., 2016, 2018; Andrews, et al., 2017; Do Campo et al., 2018; Kelson et al., 2018). However, most of the studies that have focused on terrestrial sections have been carried out in the Northern Hemisphere (Koch et al., 1995, 2003; Kraus, 1997; Domingo et al., 2009; Hyland and Sheldon, 2013; Bataille et al., 2016; Kelson et al., 2018; Song et al., 2018; Willard et al., 2019), and only a few in South America (Krause et al., 2010; Hyland and Sheldon, 2015, 2017; Andrews et al., 2017).

The Santa Barbara Subgroup (Salta Group) represents an interesting case study to ascertain the changes in paleoclimate that took place in the Paleocene–early Eocene, since its upper two units, the Maíz Gordo and Lumbrera Fms, correspond to this period and provide excellent exposures in the region of Valles Calchaquíes (Fig. 1). The paleoclimatic changes that occurred during the deposition of the Maíz Gordo Fm have been the subject of several studies (del Papa, 1999; Do Campo et al., 2007, 2018; Andrews et al., 2017). By contrast, specific studies of the Lumbrera Fm have not yet been carried out, and the few existing studies have addressed this unit only briefly (del Papa and Salfity, 1999; Andrews et al., 2017; Do Campo et al., 2018). The aim of this study is thus to undertake a characterization of the clay mineral assemblages together with a sedimentological analysis of the Lumbrera Fm in several sites corresponding to the western part of the Salta Basin (northwestern Argentina). To this end, we integrate X-ray diffraction (XRD) analysis with electron microscopy images in order to understand the textural relations and origin of clays in the Lumbrera Fm and, what is more, to correlate horizontal and vertical changes in clay mineral assemblages with global paleoclimate changes taking place during the early Eocene.

The formation of clay minerals at the earth's surface proceeds by weathering and authigenic reactions that depend on the complex interplay of a number of variables, including climate, source-area lithology, continental morphology, and the depositional environment (Chamley, 1989). However, if these variables remain constant for enough time the genesis of clay minerals will be mainly controlled by weathering intensity, which is in turn controlled by climatic conditions. When this occurs, clay minerals reach a state close to equilibrium with their environment and are thus representative of the climatic conditions prevailing during their formation in soil profiles (Thiry, 2000). For these reasons, clay mineral assemblages of continental sequences have been successfully used to infer paleoclimatic and paleoenvironmental conditions in Mesozoic and Cenozoic strata (e.g., Ruffell et al., 2002; Raucskik and Varga, 2008; Bauluz et al., 2014; Do Campo et al., 2018 and references therein).

Under dry and cold climates physical weathering prevails, generating clay mineral assemblages dominated by illite and/or chlorite. Under warm climate conditions with alternating humid and dry seasons, chemical weathering is moderate giving rise to smectite formation (Buurman et al., 1988; Güven, 1988; Chamley, 1989; Murakami et al., 1996). By contrast, humid subtropical to tropical climates are related with highly hydrolytic conditions that in turn promote kaolinite formation in sediments and soil profiles (Chamley, 1989; Righi and Meunier, 1995). Kaolinite usually forms through the dissolution of aluminosilicates such as feldspars or micas in the presence of water, and these reactions are enhanced by high temperatures and low pH, because under acid conditions silica will pass into the aqueous solution more than alumina (Velde, 1992). In view of the contrasting climatic conditions that favor illite and kaolinite genesis in weathering profiles, Chamley (1989) proposed the kaolinite/mica ratio (Kln/Ms), calculated from their relative abundances, as a paleoclimate proxy.

However, syn-sedimentary volcanic events could also leave a significant mark in clay mineral assemblages, as the highly labile volcaniclastic material that ends up in a basin can easily be transformed into smectite during early diagenesis (Cuadros et al., 1999; Do Campo et al., 2010). In the case of the Salta Basin, which developed to the east of an active volcanic arc, volcanic input should be considered as a possible source material. Accordingly, standard XRD analysis was complemented with a detailed study of representative samples by scanning electron microscopy employing backscattered electron images (BSE) and secondary electron images (SE), together with established methodologies of sedimentary facies analysis. In a previous study we have demonstrated that textural and morphological analysis of fine-grained sediments by SEM is essential to discriminate between clay minerals formed through physical and chemical weathering in soil profiles and those formed by early diagenesis of volcaniclastic material (Do Campo et al., 2010).

2. METHODS AND SAMPLES

Stratigraphic sections were measured and described bed by bed in five locations: Valle Encantado, Tin Tin, and Tonco, which are situated in the Parque Nacional Los Cardones; Obelisco, which is located near Cafayate; and Luracatao–Represa, which is situated to the west in Cumbres de Luracatao (Fig. 1). The aim was to study the changes in clay mineral associations in fluvial environments. Each site was sampled taking into account the characteristics of the sedimentary facies of the Lumbrera Formation. It is worth mentioning that the Tin Tin and Obelisco sections coincide with those reported in Andrews et al. (2017).

The mineralogical composition of 87 whole rocks and clay sub-samples from the Lumbrera Fm (32 from Valle Encantado, 18 from Tonco, 18 from Tin Tin, 12 from Luracatao–La Represa, and seven from Obelisco) was analyzed by X-ray diffraction (XRD); the distribution of the samples along the stratigraphic logs is shown in Figures 2 and 3. XRD was performed with a PANalytical X'Pert Pro diffractometer (CuKα radiation, 45kV, 40mA) equipped with an X'Celerator solid-state linear detector (Department of Mineralogy and Petrology, University of Granada). Clay sub-samples (<2 μm) were prepared in accordance with the guidelines of Moore and Reynolds (1997), and the mineral intensity factors (MIF) of the same authors were employed to estimate the relative abundances of illite-mica, kaolinite, chlorite, smectite, and I/Sm mixed-layer clays. The ratio of kaolinite and illite-mica (Kln/Ms) abundances was then calculated.

We performed standard petrographic analyses to characterize the lithology and textures of the samples corresponding to the five study sections. Afterwards, sixteen samples characterized by their high kaolinite or smectite content were chosen for detailed study using field scanning electron microscopy (FESEM), employing a Carl Zeiss FESEM to obtain textural and chemical information on the clay minerals at micro and nanoscale. In the case of the backscattered electron study (BSE) and the energy-dispersive X-ray (EDS) analysis, polished thin sections were employed. The accelerating voltage used was 15Kv with a beam current of 1 nA. Atomic concentration ratios obtained by EDS were converted into formulae according to stoichiometry. Accordingly, the structural formulae of dioctahedral smectite were calculated on the basis of 22 negative charges ($O_{10}(OH)_2$).

3. GEOLOGICAL SETTING

During Cretaceous-Eocene times, an intracontinental rift basin – the Salta Basin – developed in northwestern Argentina (Salfity and Marquillas, 1994; Viramonte et al., 1999). The successions that were deposited make up the Salta Group, which consists, from base to top, of the Pirgua, Balbuena and Santa Bárbara Subgroups. The Santa Bárbara Subgroup is in turn constituted by the Mealla, Maíz Gordo, and Lumbrera formations, which comprise fluvial environments in western proximal areas and lakes in the center of the basin (for details, see del Papa and Salfity, 1999).

The uppermost Lumbrera Fm, the focus of this study, is in paraconformable contact with the underlying Maíz Gordo Fm and is unconformably covered by the overlying Quebrada de los Colorados Fm of the foreland Payogastilla Group (del Papa, 2006).

Age constraints on the units integrating the Santa Bárbara Subgroup are mainly based on biostratigraphic and palynostratigraphic studies. Land-mammal associations and palynostratigraphy indicate that the Mealla and Maíz Gordo formations date to the Selandian and Thanetian respectively, the final two stages of the Paleocene Epoch, whereas the Lumbrera Fm has been assigned to the Eocene (Pascual et al., 1981; Quattrocchio et al., 2005; del Papa et al., 2010). Moreover, in the upper ~30 m of the Maíz Gordo Fm, comprising a thick prominent paleosol section, Andrews et al. (2017) identified several prominent CIEs from -22‰ to ~-28‰, which they correlated with the PETM, thus indicating that this interval spans the Paleocene-Eocene transition.

Additionally, the mammal fossils (isotemnids) recovered from basal levels of the Quebrada de Los Colorados Fm in Luracatao Valley, as well as a maximum depositional age of ~37Ma inferred from U-Pb ages from detrital zircons at Angastaco, indicate an Eocene age for this unit, probably middle-late Eocene (Payrola et al., 2009; Carrapa et al., 2012), thus constraining the age of the Lumbrera Fm to the early Eocene. By contrast, a recent study carried out on nearby coeval sections applied paleomagnetic results to establish the bottom of the Maíz Gordo Fm in the Ypresian (Hyland et al., 2015, 2017), the first stage of the Eocene Epoch. In reply to a comment from Hyland and Sheldon (2017), however, White et al. (2017) have questioned the Hyland et al. (2017) approach to constraining their magnetostratigraphic record and therefore the age model they proposed.

4. SEDIMENTARY FACIES OF THE LUMBRERA FORMATION

The present study focuses on the fluvial environment of the Lumbrera Fm, mainly considering the fine-grained lithologies of the floodplain setting (Figs. 2, 3).

In the study area, the thickness of the Lumbrera Fm ranges from a maximum of 237 m in the Valle Encantado section to a minimum of 60 m in the Luracatao-La Represa section, with intermediate values in the Tin Tin, Obelisco, and Tonco sites (187, 169 and 121 m, respectively) (Figs. 2, 3). The Obelisco section is not shown because only control samples were taken in this locality.

The Lumbrera Fm consists of well-developed stacked channel facies interbedded with fine-grained floodplain facies (Fig. 4A). The sedimentary facies display lateral changes from west to east, with conglomerates dominating in the western sections Luracatao-La Represa (Luracatao hereafter), Tin Tin, and Tonco-La Escalera (Tonco hereafter) (Figs. 2B and 3), and sandy lithologies prevailing in the Valle Encantado section (Fig. 2). The main facies and facies associations are summarized in Table 1.

In the western area (the Luracatao and Tin Tin sections), channel-fill facies associations (FA1) are characterized by shallow lenticular geometries 2-3 m thick. They are composed of medium to fine, white to pinky conglomerates with normal gradation and trough cross-stratification (Fig. 4C). The tops of these beds display bioturbation and red to purple mottles (Fig. 4B). The fine-grained floodplain deposits (FA3) associated with the conglomerates consist of tabular, red to brown sandy siltstones to silty sandstones, massive or with bioturbation, root traces, and clay slickenside. These facies also contain carbonate nodules (Pc) (Fig. 4D) or hematite nodules (Fh) (Fig. 4E). The contacts between conglomeratic and silty facies are sharp or in a rapid transition.

In the Valle Encantado section, channel-fill facies exhibit shallow lenticular to lenticular geometries, with common gently dipping strata (FA2). Sediments consist of pinky to whitish, medium- to fine-grained sandstones with trough cross-stratification, climbing ripples, and frequent mud-clasts, arranged in 2-2.5-m-thick fining-up successions (Fig. 4F). The fine-grained floodplain facies are dominated by red, mostly parallel-laminated, sandy to clayey siltstones, with scarce clay slickenside. Contrary to those observed in the western areas, the floodplain facies lack carbonate or hematite nodules.

The lateral gradation of the facies associations from western to eastern areas displays channels dominated by bed-load sediments to mixed-load sediments. Furthermore, the rapid transition from coarse-grained channels and bioturbated tops observed in Luracatao, Tin Tin, and Tonco suggests abandonment of active channels and/or avulsion processes common in braided fluvial systems (Miall, 1996). Toward the Valle Encantado site, lenticular channels with common inclined strata geometries are dominated by mixed-load sediments, displaying a grading transition to overbank deposits. The facies association is consistent with channel belts of moderate to high-sinuosity rivers associated with cohesive floodplains, as previously interpreted (del Papa, 2006).

Recently, Andrews et al. (2017) studied the paleosols of this unit at the Tin Tin and Obelisco sections, indicating a predominance of red claystones with abundant calcic nodules and vertic structures and occasional gray mottles. They interpreted these paleosols as having formed in a relatively dry paleoenvironment and classified them as calcic vertisols in accordance with Mack et al. (1993).

5. MINERALOGY: X-ray diffraction (XRD)

Eighty-seven whole rocks and clay sub-samples (32 from Valle Encantado, 18 from Tin Tin, 18 from Tonco, 12 from Luracatao and seven from Obelisco) from the Lumbrera Fm were analyzed by XRD. The stratigraphic position of the samples corresponding to the Valle Encantado, Tonco, Tin Tin, and Luracatao sections are shown in Figures 2 and 3. The results are summarized in Tables 2 and 3.

5.1 Whole rock mineralogy

XRD analysis of bulk samples of the claystones, siltstones, and fine-grained sandstones shows quartz and phyllosilicates to be the major components in association with minor plagioclase, K feldspar, and carbonates. Plagioclase contents are low in all the samples, usually < 10%; likewise K-feldspar contents range from 2 to 7%. Calcite is absent in most of the samples or represents less than 5%, and rarely reaches 10%. The exceptions are several levels from the Tin Tin section with calcite contents from 25 to ~ 40 %, one bed from the Tonco section displaying over 50% calcite, and one level from Luracatao section showing ~ 20% calcite. Hematite is frequently present in subordinate amounts in beds of the Lumbrera Fm from all the studied sections.

5.2 Clay Mineralogy

The clay mineralogy of the samples from the Valle Encantado, Tonco, Obelisco, Tin Tin, and Luracatao sections is summarized in Tables 2 and 3, and representative XRD patterns are shown in Figure 5. The clay mineral assemblages identified in the Lumbrera Fm are commonly dominated by illite-mica or kaolinite (Figs. 5A, B), and less frequently by smectite (Fig. 5C) or illite/smectite mixed layers (I/Sm). The siltstones and fine-grained sandstones from the Luracatao section represent the latter case because they contain abundant smectite and an expandable phase that according to XRD corresponds to R0-type I/Sm with 10 to 30% smectite layers, but whose composition, as will be discussed in the next section, covers a range from R1 and R0-type I/Sm to smectite. For example, the XRD trace of the air-dried oriented mount of LUR-5 displays the characteristic reflections of illite-muscovite and kaolinite, but also a peak at 14.98 Å, whereas in the ethylene-glycol-(EG)-treated pattern this peak shifts to 16.74 Å, and reflections at 8.54 and 5.57 Å also appear, indicating R0-I/Sm (Fig. 5D). Chlorite seldom occurs as a subordinate phase in any of the sections. Substantial changes in clay mineral assemblages are observed from bottom to top in each section but also between the different sections (Figs. 2, 3).

In the Valle Encantado site, large variations in the relative abundances of kaolinite (6-79%) and illite-mica (19-91%) are observed, as indicated by the Kln/Ms ratio varying from 0.07 to 4.15. Moreover, I/Sm or rarely smectite occurs in subordinate amounts in the clay fraction (0-15%), except in the upper ~ 50 m of the section, where both phases are absent (Table 2, Fig. 2A). The fluctuations in the relative abundances of kaolinite and illite-mica along the stratigraphic section are in some cases gradual and in others abrupt. Indeed, the basal level of the Lumbrera Fm has a Kln/Ms ratio of 0.68, which is followed in a bed 7 m up-section by a sharp increase in kaolinite content, coupled with an abrupt decrease in the illite-mica percentage, giving rise to a Kln/Ms ratio of 4.15 (Fig. 2A, Table 2). Subsequently, the illite-mica relative abundances increase sharply at the expense of kaolinite in a siltstone level 3 m up-section, displaying a Kln/Ms ratio of 0.79; after this decrease, a shale bed 4 m upwards shows a Kln/Ms ratio of 1.49. The Kln/Ms ratio remains low over the next ~ 50 m and thereupon increases sharply from 0.19 to 1.03 in 17 m. Towards the top of the unit, three more segments of low Kln/Ms followed by sharp increases in the relative abundances of kaolinite are observed, displaying maximum Kln/Ms ratios of 1.54, 0.94 and 2.12, respectively (Table 2, Fig. 2A).

At the Tonco site, where illite is the most abundant clay mineral, the kaolinite content also shows ups and downs, but it remains below 40% throughout the section (Table 2, Fig. 2B). Consequently, changes in the relative abundance of kaolinite and the Kln/Ms ratio (0.16 to 0.84) are less marked than in the Valle Encantado section. Moreover, in this section I/Sm, or less frequently smectite, represents a subordinate component of the clay fraction, attaining maximum contents of 35 and 18%, respectively.

The clay assemblages identified along the Obelisco section show a similar pattern to those at the Tonco site, located northward at a similar longitude. In this case, the Kln/Ms ratio varies from 0.14 to 1.27, whereas smectite and less frequently I/Sm occur as subordinate phases (Table 3).

The clay assemblages identified at the Tin Tin section are quite different (Table 3); illite-mica is the dominant phase in most of the beds whereas kaolinite is absent in several levels or occurs in low amounts (5-19%), thus yielding Kln/Ms ratios from 0 to 0.2, except for one level with a higher value (0.64) (Fig. 3A). Furthermore, smectite is present in all the levels analyzed, representing the main phase in two cases (LUT 29a and LUT 37). Noteworthy is that the claystones and siltstones of the upper ~ 49 m of the section contain I/Sm (14-22%) in addition to smectite.

In the Luracatao site, the clay assemblages resemble those of the Tin Tin site in that kaolinite represents a subordinate phase all along the section (6-17%) (Table 3). In this site, however, the clay assemblage is dominated either by illite-mica or by I/Sm (R0)-Sm, as these vary from 31 to 76% and from 10 to 62 %, respectively (Fig. 3B).

In summary, Luracatao and Tin Tin have higher contents of Sm (+ I/S) than of kaolinite, whereas Valle Encantado, Tonco, and Obelisco have higher abundances of kaolinite than of Sm (+ I/S).

6. TEXTURAL STUDY: Scanning electron microscopy

The five samples from the Valle Encantado section (acronym LUVE) chosen for the SEM study show heterometric and heterogeneous textures with abundant detrital fragments mainly composed of quartz, K feldspar, plagioclase, and micas (muscovite and phengite) (Fig. 6A). The composition of plagioclase is $Ab_{0.7-0.8}$, whereas K feldspar displays low Na contents, indicating a probable volcanic origin. The degree of alteration of the feldspars and micas is variable, from slight to moderate in some samples (Fig. 6 A, B) to strong in others (Fig. 6D, E), with the kaolinite contents increasing accordingly. The BSE images show that the kaolinite has grown between the mica sheets (Fig. 6B, D), sometimes showing displacive precipitation along the cleavage planes, with the feldspars slightly altered, sometimes displaying corroded edges. By contrast, in the samples showing higher kaolinite contents, feldspar (both K feldspar and albite) displays corroded edges and also replacement by kaolinite (Fig. 6D, E), whereas booklets of kaolinite are common in the matrix (Fig. 6E, F). At the same time, the replacement of mica sheets by kaolinite may be partial to almost total, since in some cases only relicts of mica remain within kaolinite booklets. These rocks also show a fine-grained matrix, which according to the EDS analysis consists of K-Al-Si-rich clays, probably of illitic phase (Fig. 6A, C).

The six samples from the Tonco section (acronym LULE) and the Obelisco section (acronym LU) studied by SEM show a similar mineralogy and texture to those from Valle Encantado (Fig. 7A). Smectite is more abundant in samples from the Obelisco section than in those from the Tonco section. In this case the alteration of feldspars and micas varies from slight to moderate. In samples with slight alteration, the BSE images show that kaolinite partly replaces large mica laths, with kaolinite growth originating at grain edges leading to the characteristic fanned-out textures (Fig. 7B, C) (De Ros, 1998; Arostegui et al., 2001). Conversely, in the samples showing stronger alteration, kaolinite not only replaces mica but also partially replaces albite and occurs as booklets in the matrix (Fig. 7D). Fig. 7E shows the growth of Sm from altered K feldspar.

The seven samples from the Tin Tin section (acronym LUT) studied by SEM also show heterometric and heterogeneous textures with abundant detrital fragments mainly composed of quartz, K feldspar, albite, and micas (muscovite and phengite). In general, feldspars and quartz are scarcely altered, displaying net edges, although feldspars showing incipient alteration to smectite occasionally occur. The K feldspars usually have some Na contents ($Si_{3.0}Al_{0.9}K_{1.1}Na_{0.1}$), as is typical of high-temperature feldspars, thus indicating a probable volcanic origin. The occurrence of micron-sized idiomorphic feldspars in several samples also suggests some volcaniclastic input. In agreement with the XRD data, SEM observations show that illite is the main clay mineral in most of the samples, followed by smectite in varying proportions, whereas kaolinite is scarce or absent. Textural features indicate that illite-mica is detrital in origin, whereas smectite displays a rose-like texture in fresh cut (Fig. 7F), thus indicating an authigenic origin. Furthermore, BSE images show that kaolinite has grown between the mica sheets and also partially replaced the mica, giving rise to muscovite-kaolinite intergrowths. By contrast, in the samples where XRD shows clay assemblages dominated by smectite (LUT29A and LUT37), BSE images indicate that this smectite occurs in the matrix, or filling cracks in sub-idiomorphic quartz (Fig 7G), with feldspar crystals without evidence of alteration. If smectite does not derive substantially from the feldspars, which are scarcely altered, it likely formed through alteration of a more reactive material contained in the matrix as well as in these cracks, probably volcanic glass.

The sample from Luracatao (acronym LUR) studied at the SEM scale displays a heterogeneous texture with abundant detrital fragments, mainly quartz, K feldspar, plagioclase, and micas (muscovite and phengite), whereas the matrix is composed of clay minerals and calcite. The feldspars and quartz display net edges, with no evidence of alteration, whereas mica laths are seldom replaced by kaolinite or smectite along the edges. Morphologies typical of authigenic smectite (or I/Sm) are observed in the matrix and fully replace irregular fragments 20-30 µm long. The coexistence of fresh K feldspar fragments with abundant smectite in the matrix, along with irregular fragments totally replaced by smectite-I/Sm, suggests (Fig. 7H) that this would have formed from a highly reactive material, probably volcanic glass, all the more so as these fragments resemble glass shards. According to EDS analysis, the composition of these dioctahedral clays covers the range from R1-type I/Sm to dioctahedral smectite.

In general, the SEM study shows that the matrix of the analyzed rocks is composed of mixtures of dioctahedral clays such as illites, I/S, and smectite. Overall, the detrital silicates show a variable degree of alteration. The formation of smectite and kaolinite has been described in the SEM study from Al-K-silicates, whereas kaolinite also grows between the mica sheets. Therefore, smectite and kaolinite are authigenic and were formed by weathering processes. The presence in Luracatao of irregular fragments formed by smectite-type clays, along with the smectite-rich matrix in samples with slightly altered silicates (e.g., feldspars), suggests the crystallization of smectite from vitreous volcanic material. Illitic phases such as illite and mica would be detrital phases that resisted the weathering. The origin of the I/S phases might be a consequence of the alteration of illitic phases, or alternatively they may have formed from transformations of the volcanic smectite.

7. CHEMICAL COMPOSITION OF SMECTITE-TYPE CLAYS: X–ray dispersive analysis (EDS)

Smectites can have variable compositions depending on their genesis, unlike kaolinite, which usually has a fixed composition. For this reason, the compositional study of clays focused on smectite-type clays.

All the smectite-type clays analyzed (smectite to R1-type I/Sm) correspond to the Al-rich-dioctahedral subgroup, with K>Ca>Na in interlayer sites (Table 4). As can be seen in Figure 8A, the smectites from the Luracatao section show Fe/Fe+Mg << 0.50 and are more siliceous than those from Obelisco, Tin Tin, Tonco, and Valle Encantado, which display Fe/Fe+Mg > 0.50. On the other hand, the smectite-type clays from the Tin Tin section display a wider compositional range. The Si vs. Mg plot was employed to differentiate beidellite from montmorillonite. As can be seen in Figure 8B, the smectite-type clays from Luracatao mainly correspond to beidellite, whereas in siltstones and claystones from Tonco, Valle Encantado, and Obelisco montmorillonite prevails. The smectite-type clays from the Tin Tin section show a wide variation covering both fields. It is worth noting that smectites with lower Si contents and higher Fe/Fe+Mg ratios prevail in the sites in which kaolinite is more abundant than smectite. By contrast, smectites that show higher Si contents and lower Fe/Fe+Mg ratios correspond to sites in which smectite is more abundant than kaolinite. These compositional differences suggest that smectite-type clays from Luracatao and some of those from the Tin Tin section were formed from a different parent material than those from Valle Encantado, Tonco, and Obelisco.

8. DISCUSSION

Burial diagenesis can obliterate or even destroy the paleoclimatic signal recorded in clay mineral assemblages, so this is the first variable to be evaluated. In our case the occurrence of smectite in the basal levels of the Lumbrera Fm in the Tin Tin, Tonco, and Obelisco sections implies that these sediments were only affected by early diagenesis during their burial history. This is in agreement with previous studies indicating that the underlying Maíz Gordo Fm only underwent eogenetic diagenesis (Do Campo et al., 2007, 2018). However, I/Sm mixed layers occur in most of the levels of Valle Encantado, Tonco, and Luracatao, in the uppermost levels of the Tin Tin section, and in some levels of the Obelisco section. The vertical distribution of I/Sm along each stratigraphic column is inconsistent with an origin by burial diagenesis (Figs. 2 and 3). Moreover, most of the beds that contain I/Sm display a Kln/Ms ratio less than 1, implying low to moderate weathering and suggesting that I/Sm could have been formed by moderate chemical weathering of illitic phases, or by early alteration of highly reactive volcanic glass. The textures observed in the BSE images point to a volcaniclastic origin, as was noted in the previous section. Kaolinite and smectite present in these sediments are primary in origin, and thus the lateral and vertical changes in the clay mineral assemblages may result from changes in paleoclimate and weathering regimes, which are the first-order factors controlling sediment accumulation. Although syn-sedimentary tectonic and volcanic events can also leave a recognizable fingerprint on clay mineral assemblages, the deposition of the Lumbrera Fm corresponds with a period of tectonic calm, so only volcanic input remains as an additional variable to be considered.

Based on varying paleosol types, organic carbon isotope signatures, and chemical weathering indexes, Andrews et al. (2017) inferred a marked change in annual mean temperatures and precipitation (MAP) between the top of the underlying Maíz Gordo Fm and the basal levels of the Lumbrera Fm. Moreover, they correlated the CIEs registered in the top 30 m of the Maíz Gordo Fm with the PETM. As regards clay mineral assemblages, the basal levels of the Lumbrera Fm display a sharp decrease in kaolinite contents and in the Kln/Ms ratio in comparison with the upper levels of the Maíz Gordo Fm (Do Campo et al., 2018). Indeed, in the Tin Tin section the upper ~ 40 m of the Maíz Gordo Fm showed an average kaolinite content of 63%, with peak values of 82%, contrasting sharply with 7% in the basal level of the Lumbrera Fm in the same section, but also with the percentage observed in other sections (8 to 39%). This change in the clay mineral assemblages, already observed by Do Campo et al. (2018), was interpreted as resulting from a strong paleoclimatic change, in agreement with Andrews et al. (2017).

However, the lateral changes in clay mineral assemblages observed in the Lumbrera Fm could not have arisen from changes in climatic conditions, as at present the Valle Encantado and Tin Tin sites are located at a distance of only ~24 km, whereas the Luracatao and Tin Tin sites are ~36 km apart (Fig. 1). What is more, the fluvial styles are consistent with downslope variation from west to east, and there are no significant changes in sedimentary facies that might suggest contrasting precipitation regimes. According to their clay mineralogy, a first distinction can be made between eastern (Valle Encantado, Tonco, and Obelisco) and western sections (Tin Tin and Luracatao). In the first group one third to half of the beds, depending on the section, display kaolinite contents over 30%, in some cases representing the dominant phase in the clay assemblages.

In the western sections, by contrast, kaolinite is absent or represents less than 10% in most of the beds, or occasionally as much as 19%. What is more, in the Tin Tin section two levels display smectite contents higher than 50% (LUT-29a, LUT-37), in contrast with the clay mineralogy of the adjacent beds. At the SEM scale, evidence of smectite (or I/Sm) that originated from a parent material more reactive than crystalline feldspars or quartz was observed in samples from the Tin Tin and Luracatao sites. Namely, the occurrence of smectite filling cracks in quartz fragments showing no evidence of alteration, irregular fragments resembling glass shards totally replaced by smectite-I/Sm (Fig. 7G), as well as abundant smectite in siltstone levels containing fresh feldspar fragments, suggests that smectite-type clays must have formed from a highly reactive material, probably volcanic glass. K feldspar with minor Na contents, as well as the occurrence of euhedral K feldspar grains, indeed point to volcaniclastic input in the sediments in the western sections. Consequently, the smectite-type clays forming these sediments probably derived not only from weathering of silicates during edaphization processes, but also from early alteration of glassy volcaniclastic material. Therefore, the clay mineral assemblages of the western sections of the Lumbrera Fm are not suitable for drawing paleoclimatic inferences as the climatic signal has been obliterated by the volcaniclastic input. The distribution of smectite and kaolinite in the area may be a consequence of the heterogeneous scattering of the volcanic material both in vitreous and crystalline phases.

The fact that the smectites originated from different material precursors is reflected in their compositions. Smectite-type clays from Luracatao mainly correspond to beidellite, whereas in the siltstones and claystones from Valle Encantado and Obelisco montmorillonite prevails, and smectite-type clays from the Tin Tin section show a wide variation covering both fields. Smectites displaying lower Si contents and higher Fe/Fe+Mg ratios prevail in the sections in which kaolinite is more abundant than smectite. By contrast, smectites that show higher Si contents and lower Fe /Fe+Mg ratios correspond to sections in which smectite is more abundant than kaolinite.

SEM images revealed evidence of volcaniclastic material in samples from Luracatao, so this could be the main precursor of the smectite-type clays in this section. On the other hand, smectite-type clays from Valle Encantado, Tonco, and Obelisco must have formed from the weathering of the detrital aluminum silicates. In both cases, the smectites would be authigenic and would be the consequence of *in situ* weathering.

The wide compositional range of smectite-type clays from the Tin Tin section suggests that they correspond to a blend of smectites of different origins both through the alteration of volcanic constituents and weathering of silicates.

On the other hand, the siltstones and claystones from the eastern sections exhibit varying degrees of alteration in feldspars and micas, ranging from slight to moderate in Tonco and Obelisco to intense in the case of the Valle Encantado section. A higher degree of weathering in detrital minerals is consistent with higher kaolinite abundance. Furthermore, textural evidence indicates that the kaolinite is authigenic in origin, as BSE images of the rocks with moderate to strong weathering show feldspar fragments with corroded edges and also replacement by kaolinite, whereas booklets of kaolinite are common in the matrix. Indeed, BSE images reveal partial to almost total replacement of mica sheets by kaolinite, which sometimes shows displacive precipitation along the cleavage planes, whereas in some cases only relicts of mica remain within kaolinite booklets. Therefore, the vertical changes in the relative abundance of clay minerals observed in the eastern sections, essentially the repeated peaks in the kaolinite percentage and Kln/Ms, indicate stages of enhanced chemical weathering probably driven by paleoclimatic changes. This is most marked throughout the Valle Encantado section, which represents the most complete profile of the Lumbrera Fm, as six levels display a Kln/Ms ratio ≥ 1, in sharp contrast with the clay mineralogy of the rest of the beds (Fig. 2A). These levels probably correspond to periods of humid-subtropical to tropical climates because such are the conditions that favor kaolinite formation under near-surface/meteoric environments at a regional scale (Chamley, 1989; Hallam et al., 1991; Righi and Meunier, 1995; Ruffell et al., 2002). By contrast, the levels in between displaying abundant illite-mica (51-93%) probably formed under a relatively dry paleoclimate. Andrews et al. (2017) carried out carbon isotope analysis of organic matter from paleosol levels of the Lumbrera Fm and identified four CIEs in this unit, which they correlated with hyperthermal events occurring during the deposition of the Lumbrera Fm. The CIEs identified by Andrews et al. (2017) correlate quite well with the four beds from the base to the middle of the Valle Encantado section displaying a Kln/Ms ratio ≥ 1. Conversely, the intermediate bed showing a Kln/Ms ratio of 0.94 cannot be correlated with the CIEs recognized by these authors. Moreover, the bed from the top of the Lumbrera Fm showing a Kln/Ms of 2.12

cannot be correlated with the data from Andrews et al. (2017), as the section considered by these authors has a thickness of ~ 144 m, whereas in the Valle Encantado section it is 231 m thick.

Given the lack of absolute ages for the Lumbrera Fm, the correlation of the six hyperthermal events recorded in this succession with those identified in deep-sea cores can only be tentative. However, there are some age constraints that may be valuable. In the first place, the PETM was identified in the upper part of the underlying Maíz Gordo Fm (Andrews et al., 2017). Second, a middle-late Eocene age has been proposed for the overlying Quebrada de Los Colorados Fm based on mammal fossils and the U-Pb ages of detrital zircons (Payrola et al., 2009; Carrapa et al., 2012). In this scenario a Ypresian to probably early Lutetian age could be postulated for the Lumbrera Fm.

The PETM, recognized at the top of the Maíz Gordo Fm, is the most drastic hyperthermal episode of the Paleogene, with an increase in sea temperature of possibly up to 6 °C (Zachos et al., 2008). Subsequently, temperatures went back to their pre-PETM levels, before starting a gradual long-term warming trend that reached its maximum during the Early Eocene Climatic Optimum (EECO; ~53-49 Ma; Zachos et al., 2001, 2008; Kirtland Turner and Ridgwell, 2013; Laurentano et al., 2015, 2018; Westerhold et al., 2018; Crouch et al., 2020). This trend was punctuated by cyclic hyperthermals throughout the Ypresian stage, ETM2 and 3 being the most severe of these events, initially identified in early Eocene marine sediments (Röhl et al., 2005; Zachos et al., 2005, 2010). Afterwards, high-resolution studies of deep-sea cores identified several prominent CIEs that took place between 56 and 52 Ma and were labeled by Cramer et al. (2003) from E to L (Cramer et al., 2009; Zachos et al., 2010; Laurentano et al., 2015, 2018; Thomas et al., 2018; Westerhold, et al., 2018; Crouch et al., 2020). Subsequently, 20 additional smaller CIEs have been documented for the Ypresian to early Lutetian (56–45 Ma) based on stable isotope records from sea cores from the Demerara Rise in the equatorial Atlantic (Kirtland Turner and Ridgwell, 2013; Sexton et al., 2011). According to Crouch et al. (2020), the base of the EECO is event J (52.8 Ma, Littler et al., 2014), whereas its top has been linked with a CIE in the uppermost chron C22n dated at 49.1 Ma. This is in agreement with Westerhold et al. (2018), who consider that the EECO lasted 4.12 Ma. The hyperthermal ETM3 took place around 52.5 Ma, thus during the EECO, and temperatures were probably higher than during ETM2 (Thomas et al., 2018). The end of the EECO coincides with the onset of a long-term cooling trend evident in the benthic $\delta^{18}O$ record (Westerhold et al., 2018). Furthermore, early Eocene hyperthermal events probably triggered increases in precipitation and thus intensification of the hydrological cycle, as the amount and intensity of rainfall are controlled by global temperatures (Held and Soden, 2006; Bataille et al., 2016). Accordingly, hyperthermal events should be associated with enhanced chemical weathering due to the combined effects of higher CO_2 levels, which favor silicate alteration, and higher humidity, leading to stronger lixiviation in weathering profiles.

In light of the previous data for the Maíz Gordo Fm (Andrews et al., 2017; Do Campo et al., 2018) and the large body of evidence from the study of deep-sea cores, we tentatively correlate the basal bed of the Lumbrera Fm at the Valle Encantado section, which displays a Kln/Ms ratio of 4.15, with ETM2, and the middle level, which has a Kln/Ms ratio of 1.54, with ETM3. According to the relative abundance of kaolinite and the Kln/Ms ratio, chemical weathering was markedly stronger during ETM2 than during ETM3, implying that in this inner continental basin the paleoclimate was more humid and warmer during ETM2, in contrast with the evidence from marine sediments (Thomas et al., 2018). On the other hand, the clay mineral assemblage from the top bed of this section, which shows a Kln/Ms ratio of 2.12, is in marked contrast with the mineralogy of the basal levels of the overlying Quebrada de Los Colorados Fm, which are dominated by illite-mica with subordinate smectite, with kaolinite representing less than 10%. Based on the clay mineral assemblages, temperate semi-arid to arid paleoclimatic conditions have been inferred for this unit (Do Campo et al., 2010). This switch in paleoclimate from subtropical humid to warm and arid would thus correspond with the global changes registered in the transition from the Ypresian to Lutetian stages. Accordingly, the upper level of the Lumbrera Fm corresponds with the peak of the EECO, which was followed by a long period of deep-sea cooling (Chekar et al., 2018). The other two levels displaying a Kln/Ms ≥ 1 correspond to some of the minor hyperthermal events identified in marine records. Nonetheless, absolute ages would be required for more precise correlations.

In the Tonco section the Kln/Ms ratio also undergoes ups and downs, but the changes are less pronounced. Several beds from the base, the middle, and the top of the section display a Kln/Ms > 0.6 in contrast with the surrounding levels. The two beds from the base with Kln/Ms ~ 0.7 could be correlated with ETM2, and the bed from the top showing a Kln/Ms of 0.84 could be associated with ETM3, whereas the intermediate bed with a Kln/Ms of ~ 0.7 could correspond to one of the intermediate hyperthermal events recorded in the Valle Encantado section.

At the Obelisco site the sampling was less detailed than in the other sections, so only a few fluctuations in kaolinite percentages can be observed. Indeed, there is no evidence of ETM2, and only one level from the top of the section with a Kln/Ms ratio of 1.27 could be tentatively correlated with ETM3.

To shed light on the impact of past global greenhouse conditions on continental subtropical areas, Kelson et al. (2018) performed a study of the Tornillo Basin in Texas (USA), covering terrestrial sediments from the Paleocene to early Eocene (67 - 52 Ma, chron C30n to chron C23r). The authors performed clumped isotope analysis on pedogenic calcite nodules and determined that the average temperatures from the early Eocene were higher than those from the Paleocene (32 ± 2 and 25 ± 3 °C, respectively; Kelson et al., 2018), with the caveat that they excluded the PETM from their statistical analysis. The authors consider that this shift in temperatures at the start of the Eocene most likely relates to a contemporaneous gradual rise in the concentration of atmospheric pCO_2 (Kelson et al., 2018). According to the same authors, the Paleocene environment in the Tornillo Basin was probably subtropical and humid with year-round precipitation, whereas for the Eocene the climate models as well as sandstone sedimentology suggest more seasonal precipitation with stronger summer monsoon rainfall than during the Paleocene (Bataille et al., 2018). In the case of the

Salta Basin, several proxies including climatic transfer functions applied to paleosol levels of the Maíz Gordo Fm, along with $\delta^{13}C_{org}$ (Andrews et al., 2017) as well as clay mineral assemblages (Do Campo et al., 2018), indicate subtropical and humid paleoclimatic conditions during the upper Paleocene, in agreement with the studies of the Tornillo Basin. Clay mineral assemblages also suggest contrasting climatic condition between the Maíz Gordo and Lumbrera formations, as these exhibit average kaolinite contents of 52% and 31%, respectively. However, our data do not indicate warmer conditions for the early Eocene, as suggested for the Tornillo Basin.

9. CONCLUSIONS

The study of the clay mineralogy of the fluvial detrital rocks of the Lumbrera Fm in the western part of the Salta Basin (NW Argentina) shows the coexistence of detrital clays (illitic phases) and authigenic clays (smectite to R1-type I/Sm and kaolinite).

The authigenic clays were formed from the alteration of detrital crystalline fragments (feldspars and micas) and from the alteration of volcanic glass, which is much more reactive than the crystalline phases. The presence of different precursors for the smectite-type clays favors variable compositions, from beidellite to montmorillonite. The variable distribution of smectite and kaolinite between the different sites and the differences in smectite composition suggest a heterogeneous scattering of the volcanic material both in vitreous and crystalline phases over the study area.

This study thus shows that the relative proportions of smectite and kaolinite observed in the Tin Tin and Luracatao sites are not indicative of variable climatic conditions, since the crystallization of smectite-type clays from volcanic glass obliterates the climatic signal. On the other hand, in the case of the Valle Encantado site, where smectite-type clays are almost absent, the input of volcanic material can be inferred to have been very low (or absent). Thus, the kaolinite crystallization in this site suggests the presence of periods of humid-subtropical to tropical climate, because such conditions favor kaolinite formation under near-surface/meteoric environments at a regional scale.

The increase in the Kln/Ms ratio (4.15) in the basal bed of the Lumbrera Fm at Valle Encantado suggests the presence of cyclic hyperthermals through the Ypresian stage and can be correlated with ETM2; the Kln/Ms ratio (1.54) in the middle level can be correlated with ETM3. These are the major hyperthermal events identified in early Eocene marine sediments.

This research shows that clay mineralogy is a powerful paleoclimatic proxy in terrestrial sediments not affected by diagenetic changes.

ACKNOWLEDGMENTS

The help of Cristina Gallego with FESEM (University of Zaragoza) was essential for the present work. The authors would like to acknowledge the use of the Servicio General de Apoyo a la Investigación-SAI, University of Zaragoza. A. Baleirón prepared the samples for X-ray diffraction, and G. Giordanengo helped with the digital figures. This work was partially financed by Research Projects RTI2018-093419-B-I00 (Spanish Ministry of Science) and E18_17R (Gobierno de Aragón and the European Social Fund, Grupos Consolidados), and also by an ANCyT - PICT-2016-1274 grant to C. del Papa (Argentina). C. del Papa thanks PUE-CICTERRA 2016. The authors would also like to thank the Ministerio de Ambiente y Desarrollo Sustentable, Programa Areas Protegidas, Secretaria de Ambiente, Salta Government, and the guards of the Reserva Manejada Quebrada de las Conchas for permission to work in the Quebrada de las Conchas Park, as well as the Salta branch of the Parques Nacionales and the Parque Nacional Los Cardones.

REFERENCES

Andrews, E., White, T., del Papa C., 2017. Paleosol-based paleoclimate reconstruction of the Paleocene-Eocene Thermal Maximum, northern Argentina. Palaeogeography, Palaeoclimatology, Palaeoecology 471, 181-195.

Arostegui, J., Irabien, M.J., Nieto, F., 2001. Microtextures and the origin of muscovite-kaolinite intergrowths in sandstones of the Utrillas Formation, Basque Cantabrian Basin, Spain. Clays Clay Minerals 49, 529-539.

Bataille, C.P., Watford, D., Ruegg, S., Lowe, A., and Bowen, G.J., 2016. Chemostratigraphic age model for the Tornillo Group: A possible link between fluvial stratigraphy and climate: Palaeogeography, Palaeoclimatology, Palaeoecology 457, 277–289, https:// doi .org /10 .1016 /j .palaeo .2016 .06 .023.

Bataille, C.P, Ridgway, K.D., Colliver, L., Liu, X-M., 2019. Early Paleogene fluvial regime shift in response to global warming: A subtropical record from the Tornillo Basin, west Texas, USA. Geological Society of America Bulletin 131, 299–317. https:// doi .org /10 .1130 /B31872 .1

Bauluz, B., Yuste, A., Mayayo, M.J., Canudo, J.I., 2014. Early kaolinization of detrital Weald facies in the Galve Sub-basin (Central Iberian Chain, north-east Spain) and its relationship to palaeoclimate. Cretaceous Research 50, 214-227.

Buurman, E., Meijer, E.L., van Wijck J.H., 1988. Weathering of chlorite and vermiculite in ultramafic rocks of Cabo Ortegal, northwestern Spain. Clays and Clay Minerals 36, 263-269.

Chamley, H., 1989. Clay Sedimentology. Springer Verlag, Berlin, 623 pp.

Charles, A.J., Condon, D.J., Harding, I.C., Pälike, H., Marshall, J.E.A., Cui, Y., Kump, L., Croudace, I.W., 2011. Constraints on the numerical age of the Paleocene Eocene boundary. Geochemistry, Geophysics, Geosystems 12, Q0AA17, doi:10.1029/2010GC003426.

Clechenko, E., Kelly, D., Harrington, G., Stiles, C., 2007. Terrestrial records of a regional weathering profile at the Paleocene-Eocene boundary in the Williston Basin of North Dakota. Geological Society of America Bulletin 119, 428–442.

Cramer, B.S., Wright, J.D., Kent, D.V., Aubry, M.-P., 2003. Orbital climate forcing of $\delta^{13}C$ excursions in the late Paleocene–early Eocene (chrons C24n–C25n), Paleoceanography, 18(4), 1097, doi: 10.1029/2003PA000909.

Cramer, B.S., Toggweiler, J.R., Wright, J.D., Katz, M.E., Miller, K. G., 2009. Ocean overturning since the Late Cretaceous: Inferences from a new benthic foraminiferal isotope compilation. Paleoceanography, 24, PA4216, doi: 10.1029/2008PA001683.

Crouch, E.M., Shepherd, C.L., Morgans, H.E.G., Naafs, B.D.A., Dallanave, E. Phillips, A., Hollis, C.J. Pancost, R.D., 2020. Climatic and environmental changes across the early Eocene climatic optimum at mid-Waipara River, Canterbury Basin, New Zealand. Earth-Science Reviews 200, 102961.

del Papa C.E., Salfity, J.A., 1999. Non-marine Paleogene sequences, Salta Group, Northwest Argentina. Acta Geológica Hispánica 34, 105–122.

del Papa, C.E., 2006. Estratigrafía y Paleoambientes de la Formación Lumbrera, Grupo Salta, Noroeste Argentino. Revista de la Asociación Argentina de Geología, 61, 15-29.

del Papa, C., Kirschbaum, A., Powell, J., Brod, A., Hongn, F., Pimentel, M., 2010. Sedimentological, geochemical and paleontological insights applied to continental omission surfaces: a new approach for reconstructing Eocene foreland basin in NW Argentina. Journal of South American Earth Sciences 29, 327-345.

De Ros, L.F., 1998. Heterogeneous generation and evolution of diagenetic quartz-arenites in the Silurian-Devonian Fumas Formation of the Paran Basin, southern Brazil. Sedimentary Geology 116, 99-128.

Do Campo, M., del Papa, C., Jiménez-Millán, J., Nieto, F., 2007. Clay mineral assemblages and analcime formation in a Palaeogene fluvial–lacustrine sequence (Maíz Gordo Formation Palaeogen) from northwestern Argentina. Sedimentary Geology 201, 56-74.

Do Campo, M. del Papa, C. Nieto, F. Hongn F., Petrinovic, I., 2010. Integrated analysis for constraining paleoclimatic and volcanic influences on clay-mineral assemblages in orogenic basins (Palaeogene Andean foreland, Northwestern Argentina). Sedimentary Geology 228: 98-112.

Do Campo, M., Bauluz, B., del Papa, C., White, T., Yuste, A., Mayayo, M.J., 2018. Evidence of cyclic climatic changes recorded in clay mineral assemblages from a continental Paleocene-Eocene sequence, northwestern Argentina. Sedimentary Geology 368: 44-57.

Domingo, L., López Martinez, N., Leng, M.J., Grimes, S.T., 2009. The Paleocene Eocene Thermal Maximum record in the organic matter of the Claret and Tendruy continental sections (South central Pyrenees, Lleida, Spain). Earth and Planetary Science Letters 281, 226–237.

Galeotti, S., Moretti, M., Sabatino, N., Sprovieri, M., Ceccatelli, M., Francescone, F., Lanci, L., Lauretano, V., Monechi, S., 2017. Cyclochronology of the Early Eocene carbon isotope record from a composite Contessa Road-Bottaccione section (Gubbio, central Italy). Newsletters on Stratigraphy 50, 231–244.

Greenwood, D.R., Wing, S.L., 1995. Eocene continental climates and latitudinal temperature gradients: Geology 23, 1044–1048, https:// doi .org /10 .1130 /0091-7613 (1995)023 <1044: ECCALT>2 .3 .CO;2 .

Güven, N., 1988. Smectites. In: Bailey S.W., Hydrous Pyllosilicates. Mineralogical Society of America, Reviews in Mineralogy 19, pp 497-559.

Hallan, A., Grose, J.A., Ruffell, A.H., 1991. Paleoclimatic significance of changes in clay mineralogy across the Jurassic Cretaceous boundary in England and France. Palaeogeography, Palaeoclimatology, Palaeoecology 81, 173-187.

Held, I.M., Soden, B.J., 2006. Robust responses of the hydrological cycle to global warming.
Journal of Climate 19, 5686–5699.

Hyland, E.G., Sheldon, N.D., Cotton, J.M., 2015. Terrestrial evidence for a two-stage mid-Paleocene biotic event. Palaeogeography, Palaeoclimatology, Palaeoecology 417, 371–378.

Hyland, E.G., Sheldon, N.D., Cotton, J.M., 2017. Constraining the early Eocene climatic optimum: A terrestrial interhemispheric comparison. Geological Society of America Bulletin 129, 244–252.

Kelson, J. R., Watford, D., Bataille, C., Huntington, K. W., Hyland, E., & Bowen, G. J., 2018. Warm terrestrial subtropics during the Paleocene and Eocene: Carbonate clumped isotope (Δ47) evidence from the Tornillo Basin, Texas (USA). Paleoceanography and Paleoclimatology 33. https://doi.org/10.1029/2018PA003391.

Kirtland Turner, S., Ridgwell, A., 2013. Recovering the true size of an Eocene hyperthermal from the marine sedimentary record. Paleocenography 28, 700–712, doi:10.1002/2013PA002541.

Koch, P., Clyde, W., Hepple, R., Fogel, M., Wing, S., Zachos, J., 2003. Carbon and Oxygen Isotope Records from Paleosols Spanning the Paleocene-Eocene Boundary, Bighorn Basin, Wyoming. In: Wing, S., Gingerich, P., Schmitz, B., Thomas, E. (Eds.), Causes and Consequences of Globally Warm Climates in the Early Paleogene. Geological Society of America Special Paper 369, pp. 49–64.

Koch, P.L., Zachos, J.C., Dettman, D.L., 1995. Stable isotope stratigraphy and paleoclimatology of the Paleogene Bighorn Basin (Wyoming, USA). Palaeogeography, Palaeoclimatology, Palaeoecology 115, 61–89.

Kraus, M.J., 1997. Lower Eocene alluvial paleosols: Pedogenic development, stratigraphic relationships, and paleosol/landscape associations. Palaeogeography, Palaeoclimatology, Palaeoecology 129, 387-406.

Krause, J.M., Bellosi, E.S., Raigemborn, M.S., 2010. Lateritized tephric palaeosols from Central Patagonia, Argentina: a southern high-latitude archive of Palaeogene global greenhouse conditions. Sedimentology 57, 1721–1749.

Laurentano, V., Littler, K Polling, M, Zachos, J. C., Lourens, L. J., 2015. Frequency, magnitude and character of hyperthermal events at the onset of the Early Eocene Climatic Optimum Climate of the Past 11, 1313–1324.

Lauretano, V., Hilgen, F. J., Zachos, J. C., Lourens, L. J., 2016. Astronomically tuned age model for the early Eocene carbon isotope events: A new high-resolution $\delta^{13}C$ benthic record of ODP Site 1263 between ~ 49 and ~ 54 Ma. Newsletters on Stratigraphy 49, 383–400. https://doi.org/10.1127/nos/2016/0077

Laurentano, V., Zachos, J. C., Lourens, L. J., 2018. Orbitally paced carbon and deep-sea temperature changes at the peak of the Early Eocene Climatic Optimum. Paleoceanography and Paleoclimatology 33, 1050-1065. https://doi.org/10.1029/2018PA003422.

Littler, K., Röhl, U., Westerhold, T., Zachos, J.C., 2014. A high-resolution benthic stable-isotope record for the South Atlantic: Implications for orbital-scale changes in Late Paleocene–Early Eocene climate and carbon cycling. Earth and Planetary Science Letters 401, 18–30.

Mack, G.H., Calvin, J.W., Monger, C.H., 1993. Classification of paleosols. Geological Society of America Bulletin 105, 129–136.

McInerney, F.A., Wing, S.L., 2011. The Paleocene-Eocene Thermal Maximum: a perturbation of carbon cycle, climate, and biosphere with implications for the future. Annual Review of Earth and Planetary Sciences 39, 489–516.

Miall, A.D. (1996). *The Geology of Fluvial Deposits: Sedimentary facies, Basin Analysis, and Petroleum Geology.* Springer Verlag, 582 p, Berlin.

Moore, D.M., Reynolds, R.C., 1997. X-Ray diffraction and the identification and analysis of clay minerals. Oxford University Press, New York, 378 pp.

Murakami, T., Isobe, H., Sato, T., Ohnuki, T., 1996. Weathering of chlorite in a quartz-chlorite schist. Mineralogical and chemical changes. Clays and Clay Minerals 44, 244-256.

Nicolo, M., Dickens, G.R., Hollis, C.J., Zachos, J.C., 2007. Multiple early Eocene hyper-thermals: their sedimentary expression on the New Zealand continental margin and in the deep sea. Geology 35, 699–702. http://dx.doi.org/10.1130/G23648A.1.

Pascual, R., Bond, M., Vucetich, M.G., 1981. El Subgrupo Santa Bárbara (Grupo Salta) y sus vertebrados, cronología, paleoambientes y paleobiogeografía. VIII Congreso Geológico Argentino, Actas 3: 743-758, San Luis.

Payrola Bosio, P., Powell, J., del Papa, C., Hongn, F., 2009. Middle Eocene deformation–sedimentation in the Luracatao Valley: Tracking the beginning of the foreland basin of northwestern Argentina. Journal of South American Earth Sciences 28, 142-154.

Quattrocchio, M.E., Volkheimer, W., Marquillas, R.A., Salfity, J.A., 2005. Palynostratigraphy, palaeobiogeography and evolutionary significance of the late Senonian and early Paleogene palynofloras of the Salta group, northern Argentina. Revista Española de Micropaleontología 37, 259–272.

Raucskik, B., Varga, A., 2008. Climato-environmental controls on clay minerals of the Hettangian-Bajocian succession of the Mecsek Mountains (Hungary): An evidence for extreme continental weathering during the early Toarcian oceanic anoxic event. Palaeogeography, Palaeoclimatology, Palaeoecology 265, 1-13.

Righi, D., Meunier, A., 1995. Origin of clays by rock weathering and soil formation. In: Velde, B., Origin and mineralogy of clays: clays and the environment. Springer-Verlag, Heidelberg, pp. 43-161.

Röhl, U., Westerhold, T., Monechi, S., Thomas, E., Zachos, J. C., Donner, B., 2005. The third and final early Eocene thermal maximum: Characteristic, timing, and mechanisms of the “X” event, Geological Society of America, Abstratcs and Programs, 37, 264.

Röhl, U., Westerhold, T., Bralower, T.J., Zachos, J.C., 2007. On the duration of the Paleocene Eocene Thermal Maximum (PETM). Geochemistry, Geophysics, Geosystems 8, Q12002, doi:10.1029/2007GC001784.

Ruffell, A., McKinley, J.M., Worden, R.H., 2002. Europe Comparison of clay mineral stratigraphy to other proxy palaeoclimate indicators in the Mesozoic of NW Europe. Philosophical Transactions of the Royal Society of London A 360, 675-693.

Salfity, J.A., Marquillas, R.A., 1994. Tectonic and sedimentary evolution of the Cretaceous-Eocene Salta Group Basin, Argentina. In: Salfity, J.A.,) Cretaceous Tectonics of the Andes. Springer, Braunschweig, 348 pp.

Schmitz, B., Pujalte, V., 2007. Abrupt increase in seasonal extreme precipitation at the Paleocene Eocene boundary. Geology 35, 215–218.

Sexton, P.F., Norris, R.D., Wilson, P. a., Pälike, H., Westerhold, T., Röhl, U., Bolton, C.T., Gibbs, S.J., 2011. Eocene global warming events driven by ventilation of oceanic dissolved organic carbon. Nature 471, 349–352. https://doi.org/10.1038/nature09826.

Sluijs, A., Bowen, G.J., Brinkhuis, H., Lourens, L.J., Thomas, E., 2007. The Palaeocene-Eocene Thermal Maximum super greenhouse: biotic and geochemical signatures, age models and mechanisms of global change. In: Williams, M., Haywood, A.M., Gregory, F.J., Schmidt, D.N. (Eds.), Deep-Time Perspectives on Climate Change: Marrying the Signal from Computer Models and Biological Proxies. The Micropalaeontological Society, Special Publications. The Geological Society, London, pp. 323–349.

Song, B., Zhang, K., Zhang, L., Ji, J., Hong, H., Wei, Y., Xu, Y., Algeo,T.J., Wang, C., 2018. Qaidam Basin paleosols reflect climate and weathering intensity on the northeastern Tibetan Plateau during the Early Eocene Climatic Optimum. Palaeogeography, Palaeoclimatology, Palaeoecology 512, 6-22.

Thiry, M., 2000. Palaeoclimatic interpretation of clay minerals in marine deposits: an outlook from the continental origin. Earth-Science Reviews 49, 201–221.

Thomas, E., 1998. The biogeography of the late Paleocene benthic foraminiferal extinction. In M.-P. Aubry, S. Lucas, & W. A. Berggren (Eds.), Late Paleocene-early Eocene biotic and climatic events in the marine and terrestrial records (pp. 214–243). New York: Columbia University Press.

Thomas, E., Zachos, J. C., 2000. Was the late Paleocene thermal maximum a unique event? GFF, 122, 169–170.

Thomas, E., Boscolo-Galazzo, F., Balestra,B., Monechi, S., Donner, B., Röhl, U., 2018. Early Eocene Thermal Maximum 3: Biotic Response at Walvis Ridge (SE Atlantic Ocean). Paleoceanography and Paleoclimatology, 33. https://doi.org/10.1029/2018PA003375.

Viramonte, J.G., Kay, S.M., Becchio, R., Escayola, M., Novitski, I., 1999. Cretaceous rift related magmatism in central-western South America. Journal of South American Earth Sciences 12, 109–121.

Westerhold, T., Röhl, U., Raffi, I., Fornaciari, E., Monechi, S., Reale, V., Bowles, J., Evans, H.F., 2008. Astronomical calibration of the Paleocene time. Palaeogeography, Palaeoclimatology, Palaeoecology 257, 377–403.

Westerhold, T., Röhl, U., Donner, B., Zachos, J.C., 2018. Global extent of early Eocene hyperthermal events: a new pacific benthic foraminiferal isotope record from Shatsky Rise (ODP Site 1209). Paleoceanography and Paleoclimatology Paleoceanography and Paleoclimatology 33, 626–642. https://doi.org/10.1029/2017PA003306.

White, T., del Papa, C. Andrews, E., 2017. Chronostratigraphy of Paleogene strata, Salta Basin, northwestern Argentina: A reply to Hyland and Sheldon's comment. Palaeogeography, Palaeoclimatology, Palaeoecology (in press).

Willard, D.A., Donders T.H., Reichgelt, T., Greenwood, D.R., Sangiorgi, F., Peterse, F., Nierop, K.G.J., Frieling, J., Schouten, S., Sluijs, A., 2019. Arctic vegetation, temperature, and hydrology during Early Eocene transient global warming events. Global and Planetary Change 178, 139–152.

Zachos, J.C., Gerald, R., Dickens, G.R., Zeebeet, R.E., 2008. An early Cenozoic perspective on greenhouse warming and carbon-cycle dynamics. Nature 451, 279-283.

Zachos, J. C., McCarren, H., Murphy, B., Röhl, U., Westerhold, T., 2010. Tempo and scale of late Paleocene and early Eocene carbon isotope cycles: Implications for the origin of hyperthermals. Earth and Planetary Science Letters 299, 242–249.

Zachos, J.C., Lohmann, K.C., Walker, J.C.G., Wise, S.W., 1993. Abrupt climate change and transient climates during the Paleogene: a marine perspective. The Journal of Geology 101, 191–213.

Zachos, J., Pagani, M., Sloam, L., Thomas, E., Billups, K., 2001. Trends, rhythms, aberrations in global climate 65 Ma to present. Science 292, 686–693.

Zachos, J.C., Röhl, U, Schellenberg, S.A., Sluijs, A., Hodell, D.A., Kelly, D.C., Thomas, E., Nicolo, M., Raffi, I., Lourens, L.J., McCarren, H., Kroon, D., 2005. Rapid acidification of the ocean during the Paleocene-Eocene Thermal Maximum. Science 308, 1611–1615.

Zeebe, R., Ridgwell, A., Zachos, J., 2016. Anthropogenic carbon release rate unprecedented during the past 66 million years. Nature Geoscience 9, 325–329.

Figure and Table captions

Figure 1. Satellite image of northwestern Argentina with rectangles outlining the location of geological maps and black stars showing the location of stratigraphic sections. A) Geological map of the Valle Encantado, Tin Tin and Tonco areas. B) Geological map of the Luracatao area. C) Geological map of the Obelisco area. Geological maps A and C were modified from Vergani and Starck (1989), and B from Payrola Bosio et al. (2009).

Figure 2. Measured stratigraphic sections and clay mineralogy of the fine-grained fraction based on XRD results. A) Valle Encantado site. B) Tonco-La Escalera site. Levels displaying peak Kln/Ms ratios mentioned in the text are indicated with arrows.

Figure 3. Measured stratigraphic sections and clay mineralogy of the fine-grained fraction based on XRD results. A) Tin Tin site. The arrow indicates a bed displaying the highest Kln/Ms ratio, further details in the text. B) La Represa-Luracatao site.

Figure 4. Field photographs of the Lumbrera Fm showing characteristic aspects of channel-fill facies and fine-grained floodplain facies at (A) Luracatao; solid square detail shown in (D), and (B) Tonco, note the person for scale. C) Conglomerate grading to sandstones with trough cross-stratification (Gt-St facies). D) Close-up view of a calcic-rich paleosol level (Pc facies) interbedded in floodplain fines at Luracatao. E) Grey to yellowish mudstone level denoting hematite formation (Ph facies). F) Sandy channel-fill facies displaying normal gradation to overbank sedimentation. Arrow indicates mudstone level sampled, Valle Encantado.

Figure 5. XRD patterns of air-dried and ethylene-glycol-solvated clay fractions of representative samples. A) LUVE27. B) LUVE32. C) LUT37. D) LUR5.

Figure 6. SEM/BSE images of samples from Valle Encantado. A) Textural image (LUVE-13) showing heterometric texture with detrital Qtz, KF, Ms, and fine-grained clay matrix. B) Kln-Ms intergrowths and kaolinite (Kln) booklets (LUVE-2). C) Clay-rich matrix and detrital KF, Qtz and Ms. D) Kln/Ms intergrowths, altered KFand Qtz fragments. E) and F). Authigenic Kln booklets and altered Ab and KF.

Figure 7. SEM/BSE images. A) Textural image (LULE-16) showing heterometric texture with detrital fragments of Qtz, KF, Ab, Ms and fine-grained clay matrix. B) Sample LULE-25 with Kln-Ms intergrowths and sparitic calcite cementing the rock. C-D) Abundant detrital fragments of silicates and Kln-Ms intergrowths (sample Lu9a). E) Growth of smectite from altered KF in sample LU29a. F) Smectite flakes forming the clay matrix of LUT39. G) Smectite filling cracks in quartz in sample LUT29a. H). Anhedral fragments formed by smectite flakes.

Fig. 8. SEM/EDS analyses of smectites. A) Fe/Fe+Mg vs Si (apfu). B) Mg (apfu) vs. Si (apfu).

Table 1. Facies association identified in the Lumbrera Formation**.** Codes from Miall (1996).

Table 2. Clay mineralogy of samples from the Valle Encantado and Tonco sites based on XRD analyses. Kln/Ms values highlighted in grey correspond to peak values mentioned in the text and marked with arrows in Figure 2.

Table 3. Clay mineralogy of samples from the Obelisco, Tin Tin, and Luracatao sites based on XRD analyses. Kln/Ms values highlighted in grey correspond to peak values mentioned in the text and marked with an arrow in Figure 3.

Table 4. Average composition of smectite-type clays (smectite to R1-type I/Sm) according to EDS microanalyses. Σoct: Sum of octahedral cations, F/FM= Fe/(Fe+Mg).

Figure 1

Click here to access/download;Figure;Figure 1 Geol map.tif

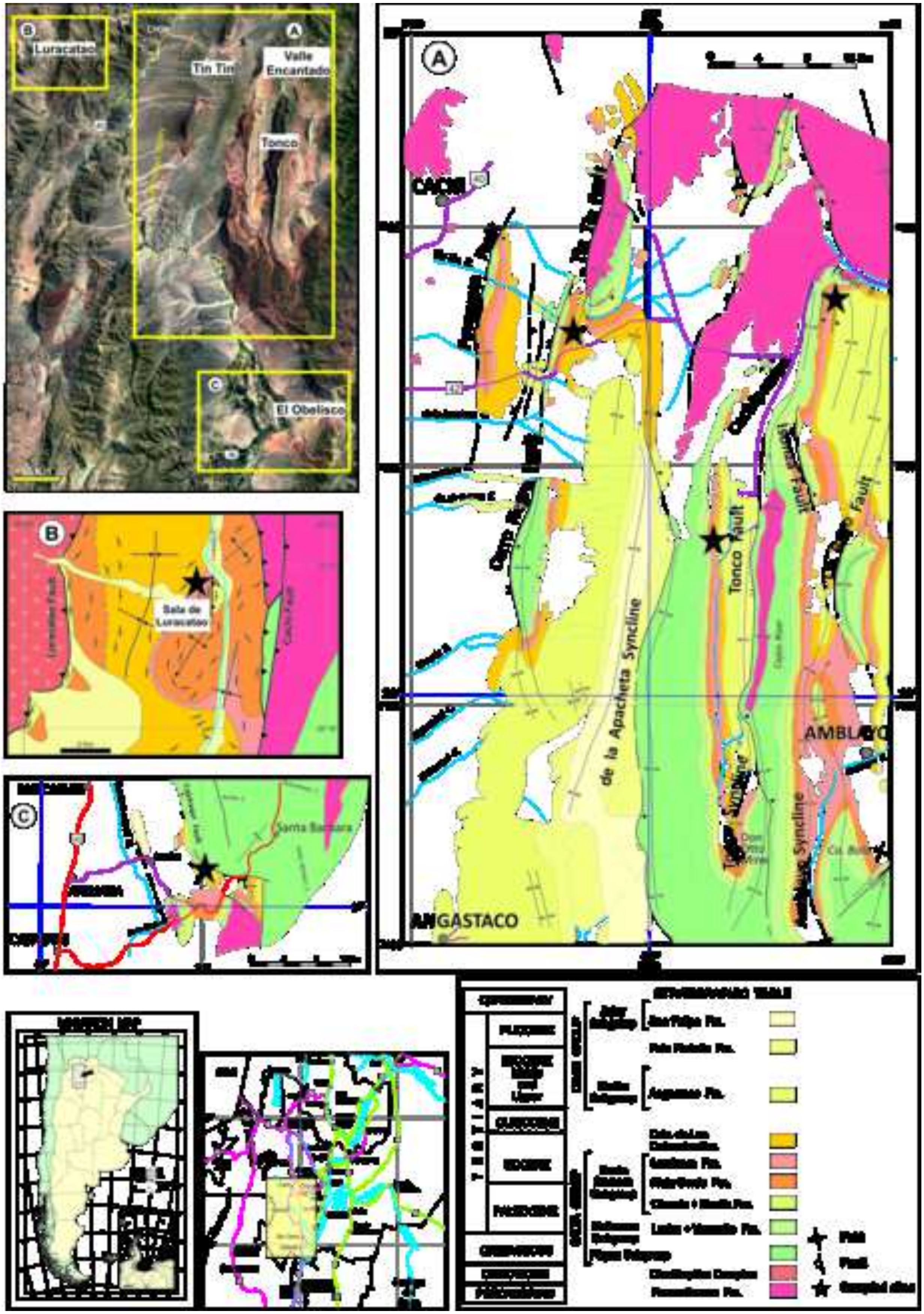

Figure 2

Click here to access/download;Figure;Figure 2 Valle Encantado and tonco log.tif

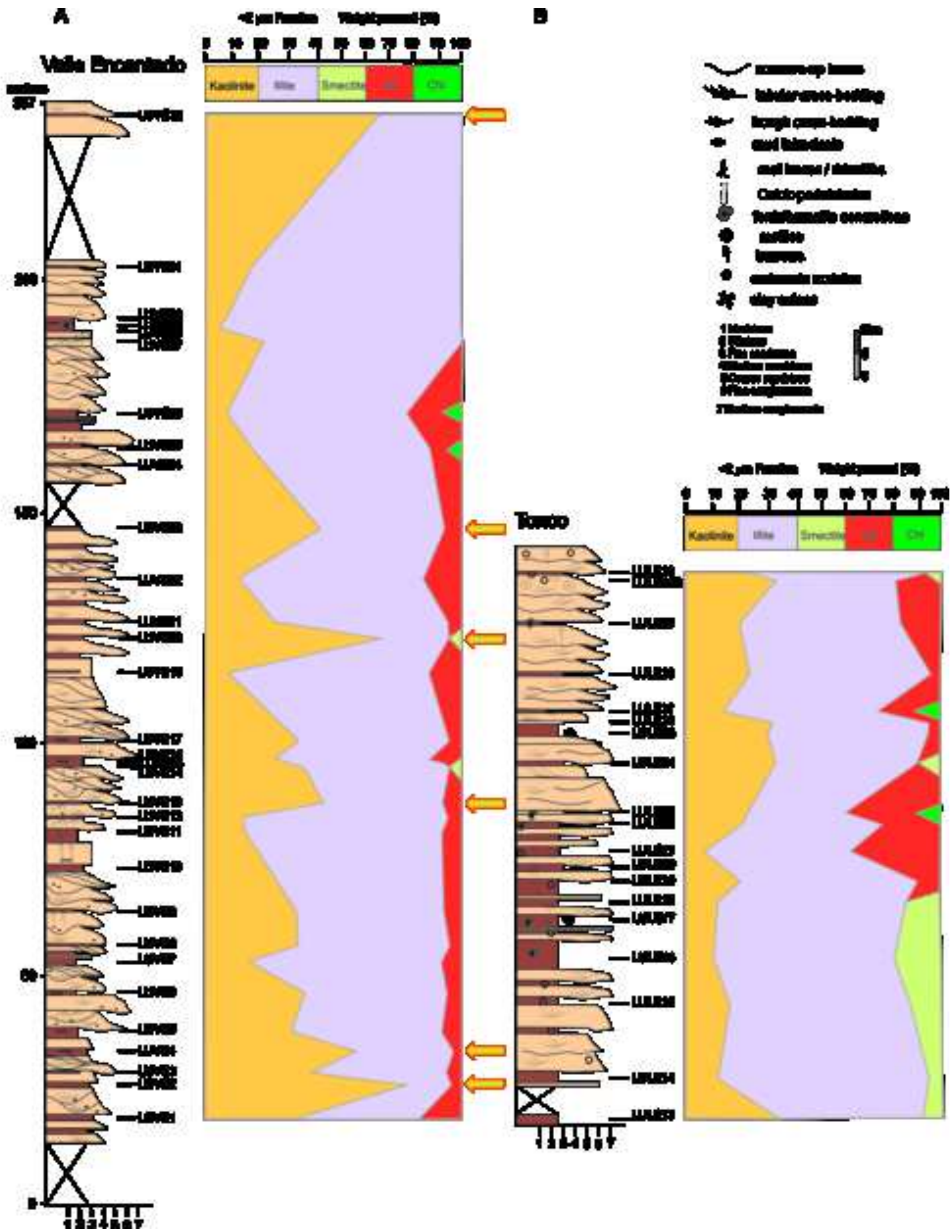

Figure 3

Click here to access/download;Figure;Figure 3 Tin Tin and La Sala log.tif

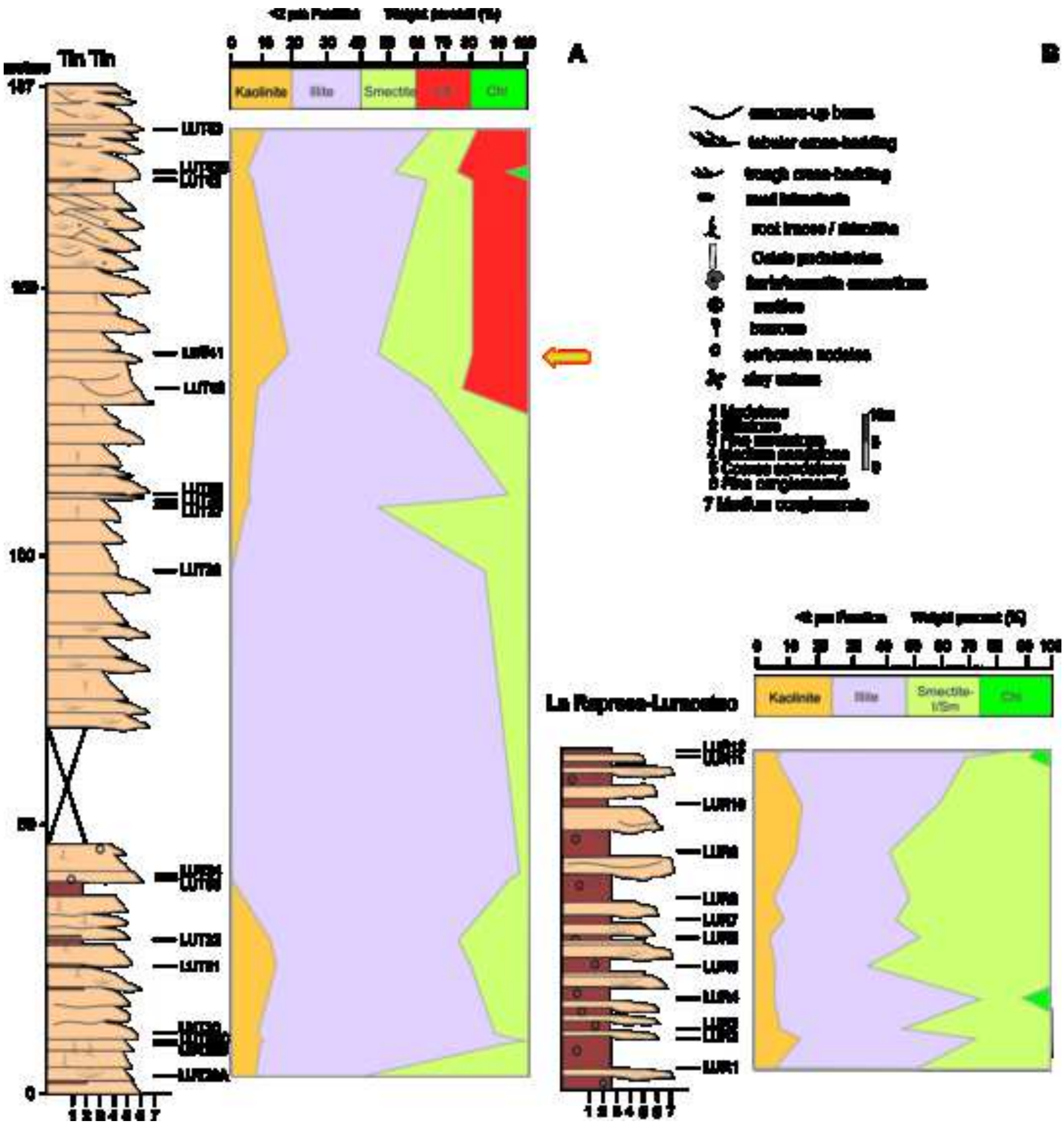

Figure 4

Click here to access/download;Figure;Figure 4.tif

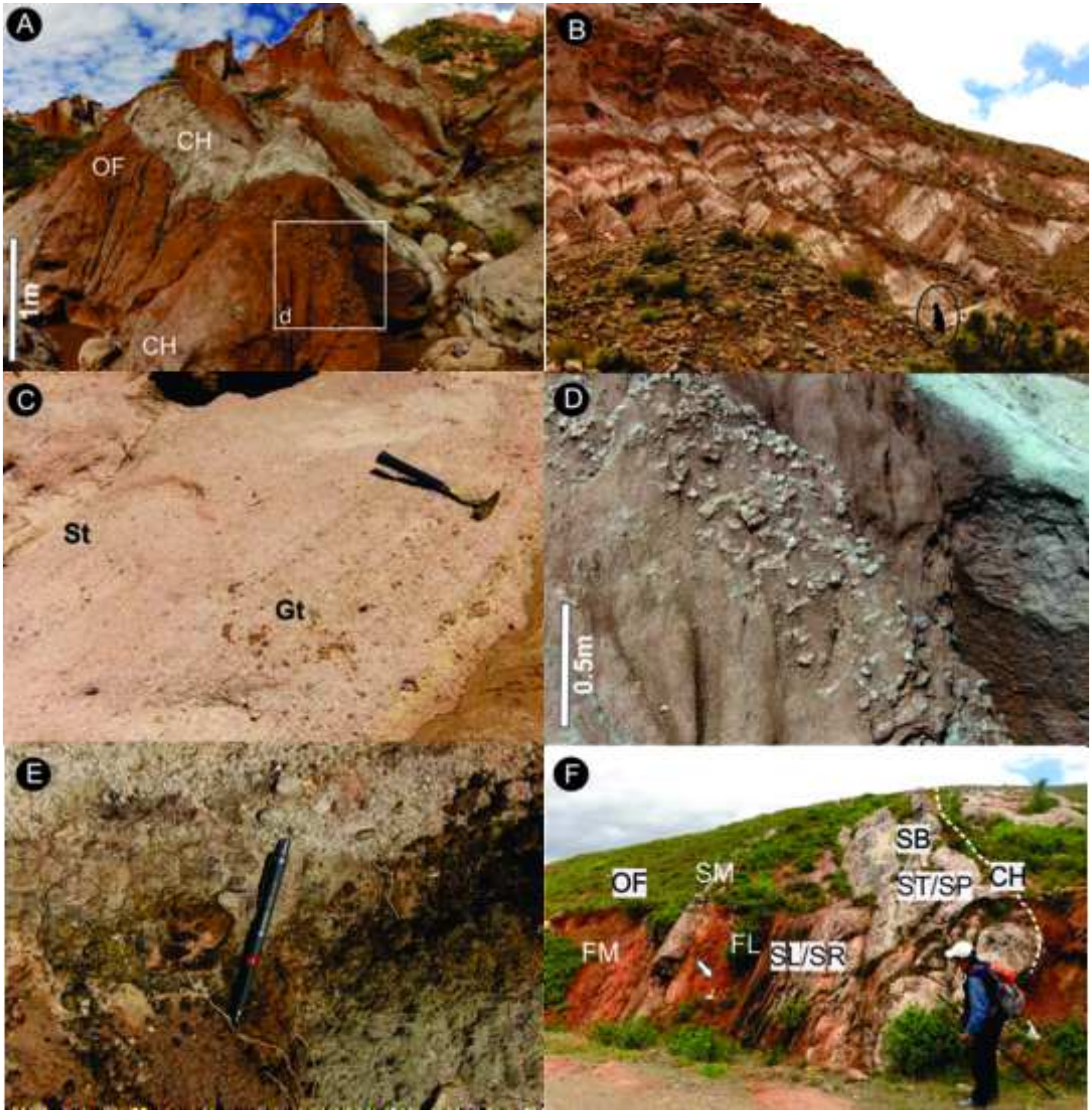

Figure 5

Click here to access/download;Figure;Figure 5.tif

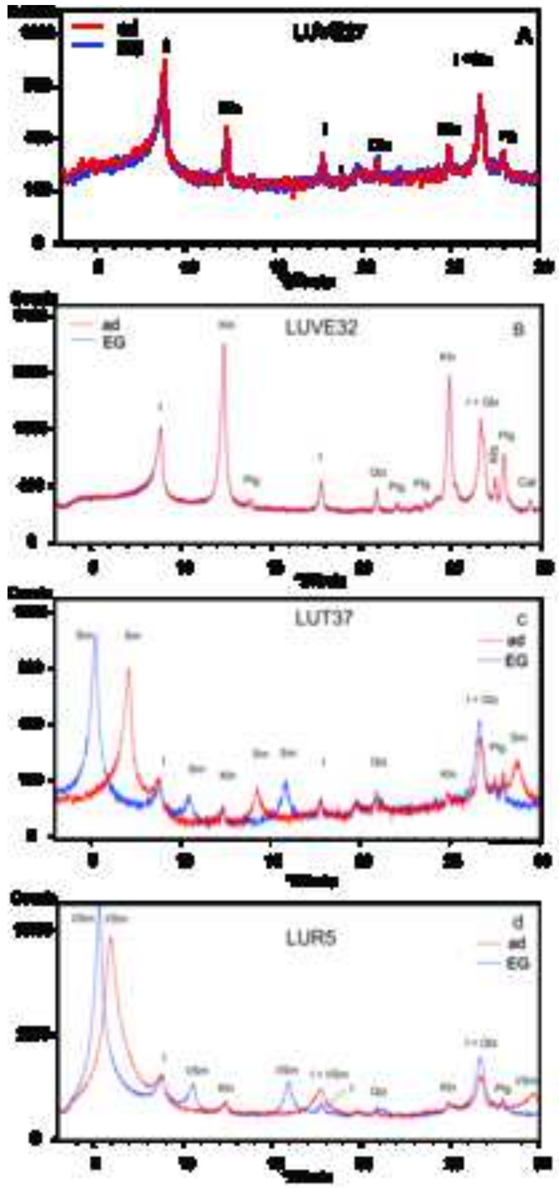

Figure 6

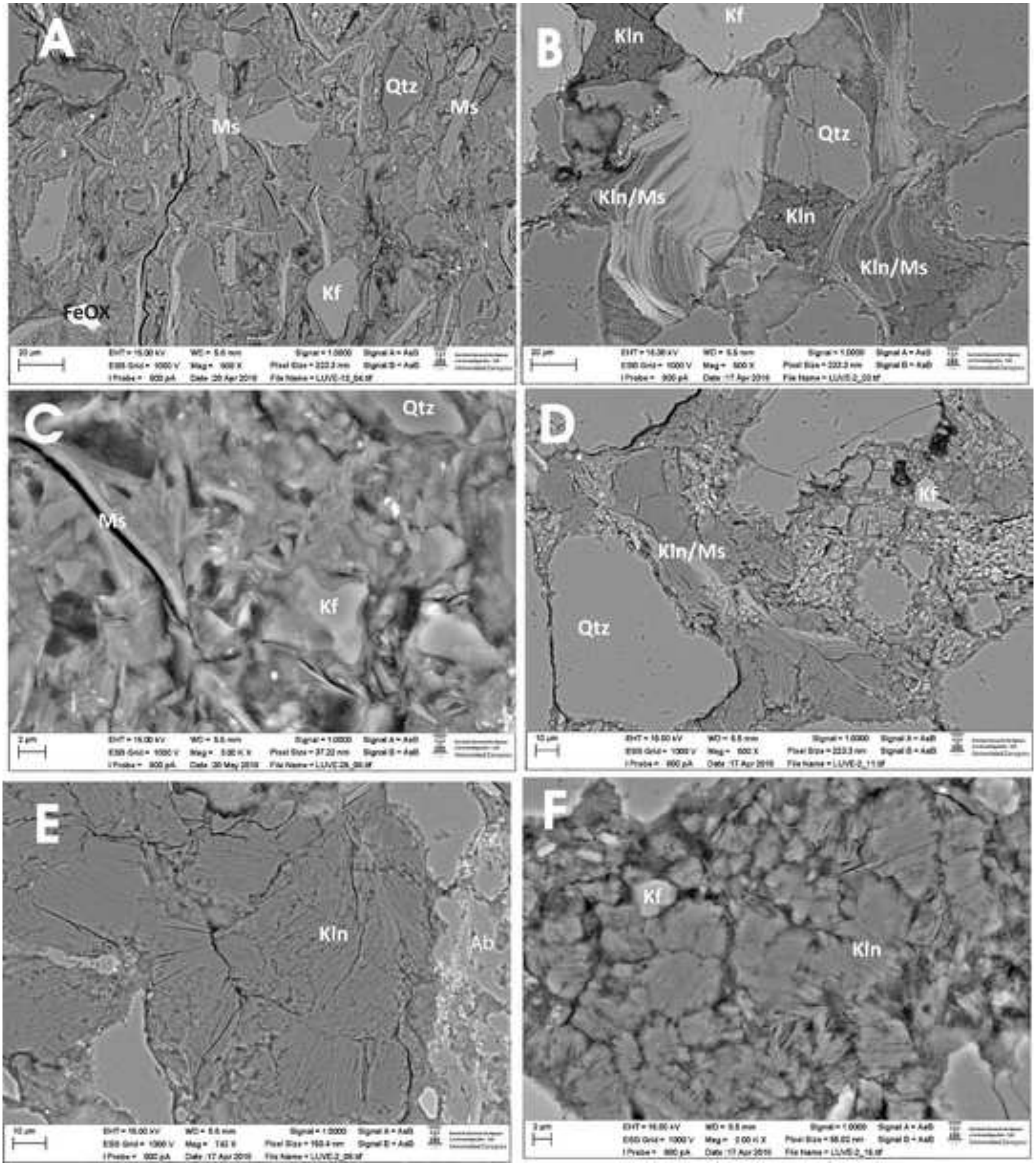
A
Qtz
Ms
Ms
Kf
FeOX
B
Kf
Kln
Qtz
Kln/Ms
Kln
Kln/Ms
C
Qtz
Ms
Kf
D
Kf
Kln/Ms
Qtz
E
Kln
Ab
F
Kf
Kln

Figure 7

Click here to access/download;Figure;Fig 7.tif

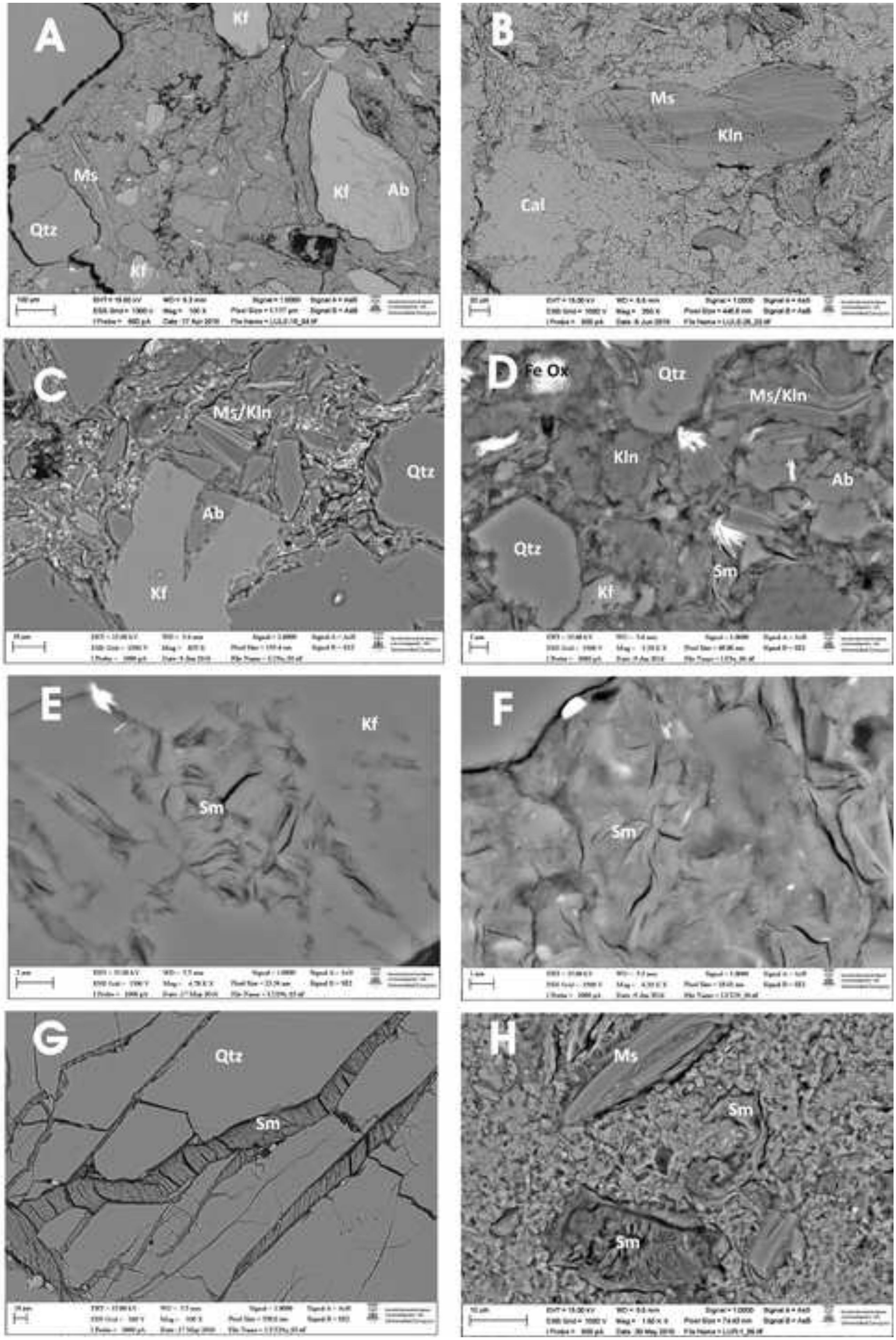

Figure 8

Click here to access/download;Figure;Figure 8 Sm composicion.jpg

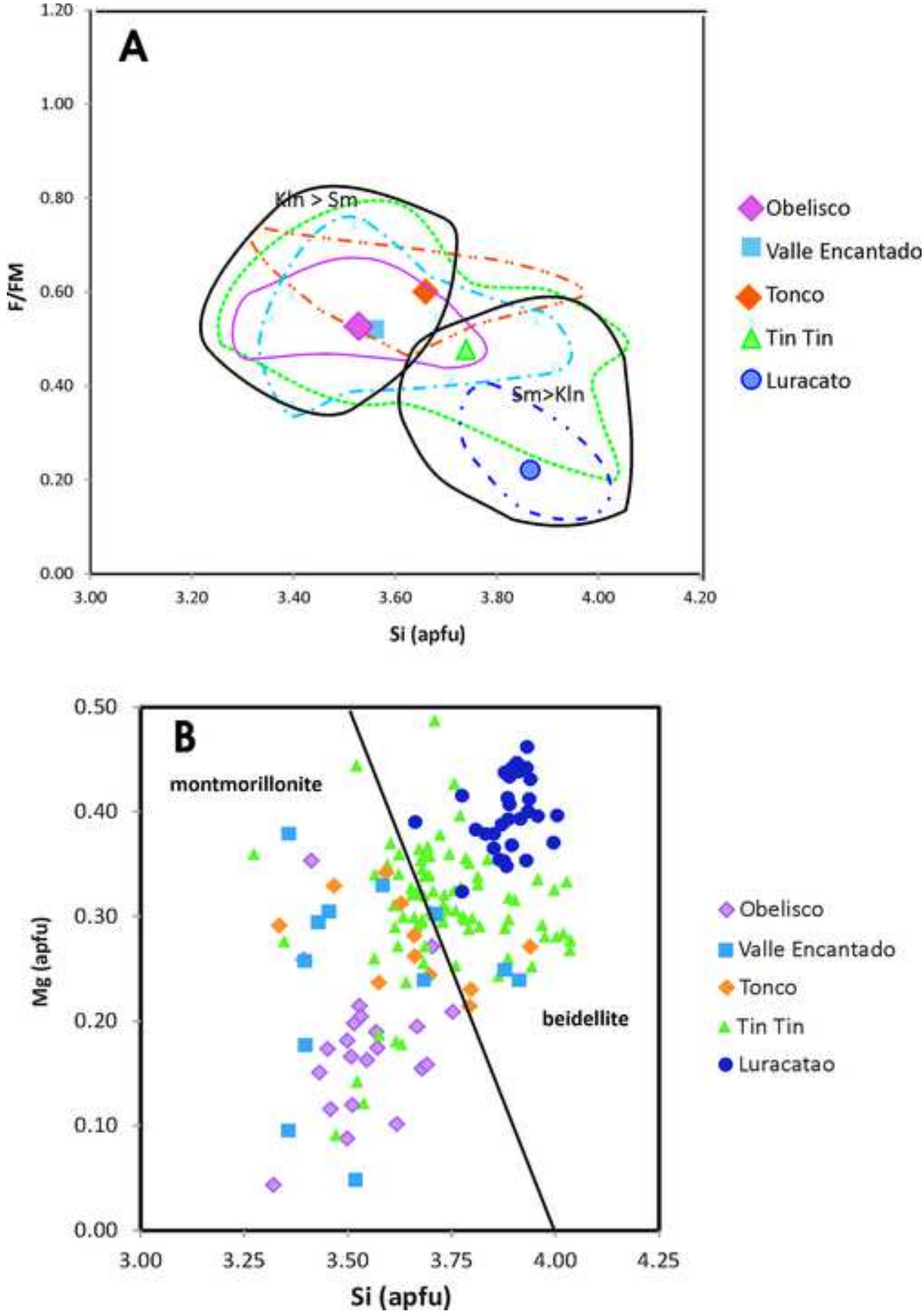

Table 1 Click here to access/download;Table;Table 1.docx

	ARCHITECTURAL ELEMENTS	FACIES	FEATURES	INTERPRETATION
FA1	CH, GB-SB	Gt, Gp, St, Sp, Sm, Fm	White to pinkish, medium to fine-granied conglomerates to gravelly sandstones. Shalow erosive bases, gravel to granule lag, nomal grading, trough cross-stratification, minor planar cross-stratification, imbrication, Bioturbated tops	Dilute currents w ith mainly tractive load. Filling scours, shallow channels, 2D-3D bar migration. Overbank sedimentation
FA2	CH, SB,LA,LV	St, Sp, Sr, Sl,Sm	Thick to thin lenticular to shallow lenticular strata. Inclined bedding. White to pinky fine to coarse-grained sandstones. Irregular bases, normal grading, trough and planar-cross stratification. Climbing ripples, some contorted beds and load casts, bioturbated tops	Belts of channels filling w ith sandy material. Mesoforms migration by lateral- and dow nstream- bar acretion. Levee formation
FA3	OF-CR	Fm, Fl,Pc, Ph, Sm	Red, massive, slightly stratified siltstones to sandy siltstones. Carbonate nodules, vertical tubes, mottling. Sheet-like, massive or bioturbated sandstones	Floodplain sedimentation, calcic-rich paleosols. Crevasse channels and splays

Table 1. Facies association identified in the Lumbrera Formation**.** Codes from Miall (1996).

Location	%	Kln	Ilite-Ms	Sm	I/Sm	Chl	Kln/Ms
Valle Encantado	LUVE 32	68	32				2.12
	LUVE 31	18	82				0.22
	LUVE 30	8	92				0.09
	LUVE 29	6	94				0.07
	LUVE 28	9	91				0.10
	LUVE 27	22	78				0.29
	LUVE 26	10	69		12	9	0.14
	LUVE 25	18	70		4	8	0.26
	LUVE 23	45	48		6		0.94
	LUVE 22	13	72		15		0.18
	LUVE 21	28	67		5		0.42
	LUVE 20	59	38	3			1.54
	LUVE 18	10	78		12		0.13
	LUVE 17	37	59		4		0.62
	LUVE 16	28	61		11		0.46
	LUVE 15	33	60		8		0.54
	LUVE 14	39	57	4			0.70
	LUVE 13	47	46		8		1.03
	LUVE 12	15	81		3		0.19
	LUVE 11	16	77		7		0.21
	LUVE 9	35	58		7		0.61
	LUVE 8	37	59		4		0.62
	LUVE 7	18	75		7		0.24
	LUVE 6	39	55		6		0.72
	LUVE 5	34	60		7		0.57
	LUVE 4	59	39		2		1.49
	LUVE 3	42	53		5		0.79
	LUVE 2	79	19		2		4.15
	LUVE 1	35	51		14		0.68

Location	%	Kln	Ilite-Ms	Sm	I/Sm	Chl	Kln/Ms
Tonco-La Escalera	LULE 30	26	68	6			0.38
	LULE 29b	38	45		18		0.84
	LULE 29	20	64		16		0.32
	LULE 28	27	70		4		0.38
	LULE 27	17	58		16	9	0.29
	LULE 26	35	62		3	0	0.56
	LULE 25	32	62		6	0	0.52
	LULE 24	36	55	9			0.66
	LULE 23	25	36		29	10	0.71
	LULE 22	23	55		22		0.41
	LULE 21	10	55		35		0.18
	LULE 19	21	70		9		0.30
	LULE 18	13	75		12		0.17
	LULE 16	11	71	18			0.16
	LULE-15	17	72	12			0.24
	LULE-14	13	83	4			0.16
	LULE-13	39	54	6			0.72
	LULE-12	39	57	4			0.69

Table 2. Clay mineralogy of samples from the Valle Encantado and Tonco sites based on XRD analyses. Kln/Ms values highlighted in grey correspond to peak values mentioned in the text and marked with arrows in Figure 2.

Location	%	Kln	Ilite-Ms	Sm	I/Sm	Chl	Kln/Ms
Obelisco	LU 10	10	70	21			0.14
	LU 9 c	36	54	10			0.65
	LU 9b	32	57	12			0.56
	LU 9a	46	36	9	8		1.27
	LU 8b	9	56		20	15	0.16
	LU 8 a	15	49		20	16	0.31
	LU 7 a	14	80	6			0.17

Location	%	Kln	Ilite-Ms	Sm	I/Sm	Chl	Kln/Ms
Tin Tin	LUT43	10	57	14	18		0.18
	LUT42b	6	49	22	14	9	0.11
	LUT42	8	60	14	18		0.13
	LUT 41	19	30	32	18		0.64
	LUT40	8	53	16	22		0.16
	LUT 39	5	88	7			0.06
	LUT 38	6	69	25			0.09
	LUT 37	5	36	59			0.14
	LUT 36	0	87	13			0.00
	LUT 35	0	89	11			0.00
	LUT 34	0	98	2			0.00
	LUT 33	0	94	6			0.00
	LUT 32	13	65	23			0.20
	LUT 31	16	65	19			0.25
	LUT 30	9	80	11			0.11
	LUT 29c	11	88	1			0.12
	LUT 29b	10	81	9			0.13
	LUT 29a	7	38	55			0.19

Location	%	Kln	Ilite-Ms	Sm-I/Sm R0	Chl	Kln/Ms
Luracatao-La Represa	LUR12	9	75	10	6	0.12
	LUR11	8	64	21	7	0.13
	LUR10	17	43	40		0.39
	LUR9	14	31	55		0.46
	LUR8	8	43	49		0.18
	LUR7	10	37	53		0.27
	LUR6	6	48	46		0.13
	LUR5	7	31	62		0.22
	LUR4	8	69	13	10	0.11
	LUR3	9	41	50		0.22
	LUR2	16	58	26		0.27
	LUR1	8	46	46		0.17

Table 3. Clay mineralogy of samples from the Obelisco, Tin Tin, and Luracatao sites based on XRD analyses. Kln/Ms values highlighted in grey correspond to peak values mentioned in the text and marked with an arrow in Figure 3.

	Si	Al IV	Al VI	Fe	Mg	Ti	K	Ca	Na	Int. charge	Soct	F/FM
Obelisco (n=23)	3.53	0.47	1.64	0.21	0.19	0.03	0.23	0.07	0.03	0.40	2.05	0.53
st.dv.	(0.12)	(0.12)	(0.21)	(0.10)	(0.10)	(0.02)	(0.09)	(0.03)	(0.02)	(0.10)	(0.05)	(0.05)
Tin Tin (n=84)	3.73	0.27	1.35	0.32	0.31	0.03	0.27	0.11	0.03	0.52	2.01	0.49
st.dv.	(0.15)	(0.15)	(0.16)	(0.14)	(0.07)	(0.02)	(0.09)	(0.03)	(0.03)	(0.07)	(0.06)	(0.13)
Tonco (n=15)	3.66	0.34	1.30	0.42	0.27	0.03	0.35	0.06	0.03	0.46	2.02	0.60
st.dv.	(0.16)	(0.16)	(0.12)	(0.12)	(0.04)	(0.02)	(0.04)	(0.03)	(0.03)	(0.09)	(0.05)	(0.06)
V.Encantado (n=15)	3.56	0.44	1.49	0.26	0.24	0.04	0.38	0.04	0.09	0.55	2.03	0.52
st.dv.	(0.19)	(0.19)	(0.22)	(0.11)	(0.09)	(0.03)	(0.10)	(0.01)	(0.10)	(0.06)	(0.07)	(0.09)
Luracatao (n=32)	3.87	0.13	1.54	0.03	0.39	0.11	0.12	0.12	0.03	0.40	2.04	0.22
st.dv.	(0.13)	(0.13)	(0.11)	(0.04)	(0.06)	(0.05)	(0.05)	(0.04)	(0.04)	(0.08)	(0.04)	(0.08)

Table 4. Average composition of smectites from the different analysed sites.

Declaration of interests

X☐ The authors declare that they have no known competing financial interests or personal relationships that could have appeared to influence the work reported in this paper.
Margarita Do Campo, Blanca Bauluz, Cecilia del Papa, Patricio Payrola Alfonso Yuste, María José Mayayo.

☐The authors declare the following financial interests/personal relationships which may be considered as potential competing interests:
